

Hubble Space Telescope Images of Magellanic Cloud Planetary Nebulae¹

Richard A. Shaw, Letizia Stanghellini

National Optical Astronomy Observatory, Tucson, AZ 85719

shaw@noao.edu, letizia@noao.edu

and

Eva Villaver², Max Mutchler

Space Telescope Science Institute, Baltimore, MD 21218

villaver@stsci.edu, mutchler@stsci.edu

ABSTRACT

We present images and slitless spectra which were obtained in *HST* surveys of Planetary Nebulae (PNe) in both the Large and Small Magellanic Clouds, using the Space Telescope Imaging Spectrograph. These new data on 59 PNe (54 in the LMC and five in the SMC) permit us to determine the nebular dimensions and morphology in the monochromatic light of several emission lines: $H\alpha$, $[N\ II]\ \lambda 6583$ and $[O\ III]\ \lambda 5007$, plus others of varying ionization, including $[O\ I]$, He I, and $[S\ II]$. We describe the nebular morphology and related features in detail. This survey, when combined with similar data from our prior *HST* programs and other archived PN images, brings the total of nebulae imaged with *HST* to 114 in the LMC and 35 in the SMC. We describe various basic properties for the sample, including sizes, morphologies, densities, and completeness. Trends in $[O\ III]\ \lambda 5007$ flux, surface brightness, and electron density with physical radius suggest that many nebulae, particularly those with bipolar morphology, may be optically thick even at large size. Bipolars also show the most extreme values of $[N\ II]/H\alpha$ flux ratios, which is a rough indicator N enrichment.

Subject headings: Magellanic Clouds — planetary nebulae: general – stars: evolution

²Affiliated with the Hubble Space Telescope Space Department of ESA.

¹Based on observations with the NASA/ESA Hubble Space Telescope, obtained at the Space Telescope Science Institute, which is operated by the Association of Universities for Research in Astronomy, Inc., under NASA contract NAS 5-26555.

1. Introduction

Planetary nebulae (PNe) in the Magellanic Clouds have been employed very successfully over the past few decades to investigate a number of very important astrophysical questions, including chemical abundances in the ISM of these galaxies, abundance yields of low-mass stars, the kinematical properties of the host galaxies, and even the extra-Galactic distance scale. In the past two decades a number of investigators have turned their attention to understanding the individual nebulae in detail in an effort to improve our understanding of stellar evolution, chemical enrichments, and the formation and evolution of the nebulae themselves. The effects of stellar evolution through the Asymptotic Giant Branch (AGB) on the Galactic PN abundances and on the central star (CS) mass and evolutionary paths have been well studied. However, recent modelling of the co-evolution of PNe and their central stars (Villaver, Manchado & Garcia-Segura 2002; Perinotto, et al. 2004) shows that the PN detectability and many of the observed properties of the PNe are intimately tied to the post-AGB evolution of the CS.

Planetary nebulae are in many ways complex phenomena. Theories of their origin, morphology, chemical composition, evolution, and their use in inferring the evolutionary state of their CSs are complex and generally rich in their predictive power. Exploring their validity requires samples that are well populated, volume- and flux-complete, and uniformly observed in order to assure that the full set of observable phenomena are represented. For these purposes the study of Magellanic Cloud planetary nebulae (MCPNe) is potentially ideal: the Magellanic Clouds are massive enough that large numbers of PNe are available for study; the nebulae within a given Cloud all lie at essentially the same distance; the nebulae are bright enough that high quality spectra can be obtained easily, yet they are distant enough that the whole nebula can be fit within typical spectroscopic apertures; they are near enough that they can be resolved in considerable detail with the best resolution telescopes (such as *HST* or modern ground-based telescopes with adaptive optics); and the foreground extinction is very low. What has most limited the observational study of critical nebular and CS properties (and their correlation with nebular morphology) in the Magellanic Clouds up until the beginning of this decade has been the comparatively small number of nebulae with high resolution images.

HST imagery of MCPNe began with GTO program 1046 by Blades, et al. (1992), and was followed up by more than a dozen others, which are listed in Table 1. Reference keys to papers that analyze PN properties based on the *HST* programs are given in the last column of the Table. Unfortunately, the six earliest programs were executed with the spherically aberrated *HST*, prior to the first servicing mission, which limits the utility of the data. Stanghellini, et al. (1999) summarized the observations of the 17 LMC and 10 SMC PNe from the first seven programs and expanded the analysis of these data to study the PN morphologies. More comprehensive imaging surveys followed in the next few *HST* observing cycles, most of which were conducted as SNAPSHOT programs, as described by Shaw et al. (2001, hereafter Paper I), Stanghellini, et al. (2002, hereafter Paper II), and Stanghellini, et al. (2003, hereafter Paper III). These surveys expanded the available sample to 59 PNe in the LMC and 37 in the SMC, including some PNe from prior programs that were

re-observed with STIS. The *HST* programs described in this paper, including one of LMC PNe (Cycle 9, Program 9077), and one of the SMC PNe (Cycle 13, Program 10251), extend earlier work and provide imagery on 54 LMC PNe and five SMC PNe. Other, mostly serendipitous *HST* observations from various programs have added images of another five LMC PNe and one additional SMC PN. In sum, these contributions to the *HST* archive provide the most complete dataset on extra-galactic PN morphology achieved to date, with imaging of 114 unique PNe in the LMC and 35 unique PNe in the SMC. The observational data, including the images and the emission line fluxes, are described in § 2, and the nebular dimensions, morphology, and detailed features are described in § 3. We analyze the LMC and SMC nebular properties in § 4, and summarize our conclusions in § 5.

2. Observational Data

2.1. Imaging

The data presented here from GO programs 9077 and 10251 were obtained with *HST* using the Space Telescope Imaging Spectrograph (STIS). See Woodgate, et al. (1998) for a description of the instrument, and Kimble, et al. (1998) for a description of the initial, on-orbit performance. The observing approach and instrument configuration are almost identical to that described in Paper I. Briefly, the targets were scheduled as SNAPSHOT exposures, which meant that the actual observations were selected on the basis of expediency for the telescope scheduling system, and on the availability of visits with suitable durations. All known, yet unobserved LMC PNe were potential targets for program 9077 (i.e., 224 visits were granted for program 9077), though only a modest fraction were actually observed. In practice, brighter targets with short exposure times were observed much more often than fainter targets requiring longer visits. For program 10251 where 53 visits were approved (in order to observe all SMC PNe within ~ 5 mag of the brightest), only five relatively bright targets were observed prior to the failure of the STIS instrument. This introduces a significant bias when attempting to draw conclusions about the full sample of LMC PNe (see § 4).

All of our observations were made with the CCD detector, using a gain of $1 e^-/\text{ADU}$. Most of our exposures were split into two components of equal duration to facilitate cosmic ray removal. We obtained slitless spectra with the G430M and G750M gratings which yielded monochromatic images of the target nebulae in several important emission lines. We also obtained direct, broad-band images with the clear (50CCD) aperture in order to measure central star (CS) magnitudes as faint as $V \approx 25$ with a short exposure, and to distinguish between the spatial and the velocity structure in rapidly expanding nebulae. The fraction of CS detections with this technique is close to 65% (Villaver, Stanghellini & Shaw 2003, 2004, 2006). The observing log is presented in Table 2.

The calibration procedure is nearly identical to that described in Paper I, except that more recent versions of the processing software were employed. The instrumental signature was removed

from the images and spectral images with the STIS calibration pipeline, version 2.18 (2005 Jan.), as initially described by Hodge, et al. (1998a) and Hodge, et al. (1998b). This portion of the processing subtracts the bias, corrects for hot pixels by scaling and subtracting dark exposures, and divides by a normalized flat-field image to correct for pixel-to-pixel variations in detector sensitivity. The pipeline also combines multiple exposures, using an anti-coincidence technique to remove cosmic ray trails and other transient artifacts. A noteworthy improvement to this version of the pipeline, compared to that used for Papers I, II, and III, is the correction for charge transfer (in)efficiency (Bohlin & Goudfrooij 2003), the effects of which grow slowly in time owing to the degradation of the STIS CCD detectors in flight.

A recent search of the *HST* archive has uncovered a few images in the vicinity of known MCPNe, most of which were observed as a part of pure parallel programs. We have analyzed five additional nebulae (one of which was imaged during an acquisition for a STIS spectroscopic program) and include the results in this paper. The observing log of these other programs is presented in Table 3. These images, with the exception of that for LMC-MA 17, were calibrated with the standard reduction pipelines for the instruments used to obtain them. These pipelines perform essentially the same corrections as that for our STIS images: bias correction, dark scaling and subtraction, and flat-fielding. In addition, the ACS pipeline performs a geometric rectification. For the present purpose we are concerned primarily with determining the coordinates, sizes, and morphologies of these nebulae, so that the accuracy of the reductions is not so important. However we did combine images taken with the same filter, when available, to eliminate cosmic rays and to improve the signal-to-noise ratio for presentation.

2.2. Spectroscopy

Extraction of one-dimensional spectra from the STIS two-dimensional spectral images proceeded similarly to that described in Paper II. For this purpose we used the X1D module of the STIS pipeline (McGrath, Busko, & Hodge 1999); the key parameters that define the extraction (the position and size of the extraction window) are given in Table 4. A noteworthy improvement to this module since Papers II and III were published was the implementation of a correction for the slow degradation of the detector sensitivity with time (Stys, Bohlin & Goudfrooij 2004). Prior to extraction, the two-dimensional images were filtered to remove image artifacts, such as the effects of extreme charge traps (pixel values below -25 electrons) and incomplete corrections for hot pixels (isolated pixels with values of a few hundred electrons above that for adjacent pixels) in the immediate vicinity of emission features. These corrections to tens to perhaps a few hundred pixels have no effect on the flux calibration, but do have the effect of improving the realized signal-to-noise ratio in the extracted spectra for weak emission features. The fluxes from each of the detected

emission lines were measured from the extracted spectra using the IRAF² task **splot**. All of the fluxes were measured via direct integration above the local continuum, rather than assuming an intrinsic (e.g., Gaussian) shape to the emission profile, because of the often complex spatial profile of the nebulae.

The emission line intensities are presented in Table 5, uncorrected for interstellar reddening, and are normalized to $F(\text{H}\beta)=100$. Column 1 gives the nebula name using the widely-used designation of Sanduleak, MacConnell & Phillip (1978) where possible, and otherwise by the original discovery catalog (Jacoby 1980; Sanduleak 1984; Morgan & Good 1992; Morgan 1994). Column 2 gives the log of the flux in $\text{H}\beta$ $\lambda 4861$ in $\text{erg cm}^{-2} \text{s}^{-1}$, and column 3 gives the extinction constant, c (the logarithmic extinction at $\text{H}\beta$) as computed from our $F(\text{H}\alpha)/F(\text{H}\beta)$ ratio and assuming an electron temperature of 10,000 K and density of 10^4 cm^{-3} . The intensities for the bright nebular emission lines, relative to $\text{H}\beta = 100$, are given in columns 4 through 14. Blends of emission lines that occur for large nebulae are noted in the table, in which case the sum of the line intensities in the blend is given.

We expect the accuracy and associated uncertainties of our relative fluxes to be very similar to those described in Papers II and III, since the techniques for spectral extraction, calibration and flux measurement are nearly identical. Since the sample of Magellanic Cloud PNe presented here and in Papers II and III is now fairly large it is useful to compare our absolute fluxes to those in the literature, all of which are from ground-based data. We present in Figure 1 a comparison of the published fluxes with ours in the $[\text{O III}] \lambda 5007$ emission line (scaling by the published absolute flux in $\text{H}\beta$ where necessary). The sample of MCPNe in common spans about two orders of magnitude in flux. Usually the agreement is very good, though in several cases (particularly for log fluxes less than -12.75) the agreement is poor. Some objects which were observed by more than two investigators are connected by thin vertical lines. In these cases it is clear that most of the most discrepant values are inaccurate.

Of all the published fluxes with targets in common, those of Boroson & Liebert (1989) cover the largest dynamic range. On the whole the agreement is good, but the deviations for individual nebulae are sometimes more than a factor of three, almost independent of the brightness. Objects in common with Meyssonnier (1995) also show good agreement over a wide range, except for one extremely discrepant object (SMC–J 23) where the difference is a factor of 100. The greatest overlap of objects is with Jacoby, Walker & Ciardullo (1990, hereafter, JWC) where the agreement for objects brighter than -13 in the log is excellent, apart from a consistent offset of about 10%, as shown in Figure 2. The cause of the offset, where the JWC fluxes are consistently brighter than ours, is not entirely clear. For ground-based data the principal challenges to accuracy are the photometricity of the observing conditions, and relatively large entrance apertures that can admit a considerable amount of light from background sources. The light from the background includes

²IRAF is distributed by the National Optical Astronomy Observatory, which is operated by the Association of Universities for Research in Astronomy, Inc., under cooperative agreement with the National Science Foundation.

field stars and (often) significant diffuse emission line radiation that varies with position. The STIS spectra are rather less susceptible to these particular effects, owing to the superior spatial resolution and the large effective entrance aperture (nearly $1'$ by $1'$) which both assures that no nebular light is lost, while spreading the background diffuse emission over the whole detector. It is possible to exclude light inadvertently from the STIS spectra by using virtual extraction slits that are too small. In this case we would expect to see fluxes that agree with those of JWC for small, nearly unresolved nebulae (owing to the well calibrated correction in the STIS pipeline for finite-aperture effects), but that become systematically too small for large nebulae, which we do not find. In any case, the systematic offset is far larger than uncertainty in the measurement errors claimed by JWC, and also larger than that for the absolute accuracy of STIS in this mode (a few percent). We conclude that the fluxes from this paper, Papers II and III in this series, and those of Jacoby, Walker & Ciardullo (1990) and Jacoby & Kaler (1993) are the most consistent and likely the most reliable for log fluxes greater than -12.75 ; below that value our fluxes are probably the most reliable to date.

3. Dimensions and Morphology

The broad-band, [O III] $\lambda 5007$, and $H\alpha$ $\lambda 6563$ + [N II] $\lambda\lambda 6548, 6583$ images for the target nebulae of program 9077 are presented in Figures 4 through 16, and in Figure 17 for the SMC nebulae of program 10251. Images of PNe from the other *HST* programs are presented in Figure 18. All of the data are rendered as grey-scale images, usually with a log intensity scale in order to bring out the often faint structural features.³ We classified the morphologies in our sample on the basis of the [O III] $\lambda 5007$ monochromatic images in the G430M spectra (although we were guided by the $H\alpha$ and [N II] $\lambda 6583$ images), using the same classification scheme as in Papers I and III. The morphological types are: round (R), elliptical (E), quadrupolar (Q), point-symmetric (P), bipolar (B), and the sub-class of bipolar-core (BC). The BC designation is applied to nebulae that have a round or elliptical outer contour, but also have internal structure in the form of two lobes of emission that surround the center, and that are at least 20% brighter than the immediately surrounding nebula. When present, such structure is an important morphological feature, in that these nebulae may be more closely related to pure bipolar (B) PNe than either R or possibly E (see § 4, below). Our distinction between E and R was based (somewhat arbitrarily) on whether the major axis of the 10% intensity contour exceeded the minor axis by more than 10%. Other important structural features, such as attached shells, ansae, and jets were noted as well. The morphological class was assigned primarily on the basis of structures evident in the [O III] image, and would seldom have been different had we instead used another, lower-ionization line such as [N II] $\lambda 6583$. Indeed, in only one case (out of 61 resolved nebulae), for LMC-SMP 62, might the classification have been

³Cut-out, false-color images of the entire *HST* sample are available for browsing at the MAST archive, at <http://archive.stsci.edu/hst/mcpn/>.

different. We conclude that at least for the broad morphological characteristics considered here, only the [O III] $\lambda 5007$ image is essential for a correct classification with this schema. A refined classification to quantify the effects of projection may now be possible (Zhang & Kwok 1998), but a significant improvement would require spatially resolved, high-resolution spectra to understand the velocity field of the gas.

Table 6 gives detailed information for the PNe presented here. The sky coordinates are given in columns 2 and 3, and the photometric radii are given in column 4, which were derived according to the method described by Stanghellini, et al. (1999). The photometric radius, R_{phot} , corresponds to the size of a circular aperture that contains 85% of the flux in [O III] $\lambda 5007$. R_{phot} gives an objective measurement of nebular angular size which is insensitive to the S/N ratio of the image, and is useful for evolution studies. The nebular diameters, given in column 5, were measured with respect to the 10% intensity contour of the outermost structure, and are useful for conducting follow-on observations of the PNe. The morphological classification is given in column 6.

3.1. Individual Nebulae

As discussed in the previous section, we have observed 54 PNe in the LMC and five nebulae in the SMC. In addition, we have analyzed archived images of an additional five PNe in the LMC and one in the SMC. We describe in this subsection the morphological details and noteworthy spectral features for each nebula listed in Table 6. We take special note of objects that show extreme ratios of $F([\text{N II}])/F(\text{H}\alpha)$: often this occurs for large objects. In these cases the lines are partially blended (see Table 5), so that the ratio (or a limit) is determined only approximately from unblended portions of the emission.

LMC-J 5.—This nebula is an elliptical ring, though there is a knot of bright emission nearly coincident with the extremely bright central star (CS). The CS is displaced about $0'.25$ (0.06 pc) along the major axis of the ellipse, near the eastern edge of the nebula, and might have been mistaken for a field star were it not for the associated emission. The core of the CS is saturated in the broad-band image, with a V magnitude a little less than 17.6 (Villaver, Stanghellini & Shaw 2006). The nebular emission from the [N II] $\lambda 6583$ line is a few times brighter than that from $\text{H}\alpha$, and a faint extension of nebulosity can be seen to the east. The surface brightness of the knot in the broad-band is roughly five times larger than that from the rest of the nebula. The emission spectrum of the knot is different from the rest of the nebula, and is mixed with stellar emission lines. Fig. 3 shows that the bulk $\text{H}\alpha$ emission is of stellar origin. A small deficit of emission blueward of the peak, which is also present in $\text{H}\beta$ but not in the forbidden lines, suggests a P-Cygni profile. Alves, et al. (1997) found the CS to be irregularly variable, with an amplitude of up to 0.4 mag in the visible, and noted that the concomitant change in $V - R$ color was consistent with increased reddening. Boroson & Liebert (1989) noted the presence of Fe emission lines in the spectrum. The combination of morphological, temporal, and spectral features suggests that J 5 is a genuine PN with a binary CS. (See Fig. 4.)

LMC-J 33.—This slightly elliptical nebula has an attached outer shell that is almost twice the size and about one-third the surface brightness of the bright, inner nebula. The central star is easily visible. (See Fig. 4.)

LMC-MA 17.—This nebula has a quadrupolar morphology (which is very rare, and is the same as that for SMP 27), with rough dimensions of 0.215 x 0.164 pc. It has what may be jets extending about a 0.3 pc from the central star, and are symmetric along an axis that is inclined roughly 30° from the minor axis. (See Fig. 19.)

LMC-MG 4.—This is one of the largest nebulae in our sample, with very low average surface brightness that renders the morphological classification uncertain. The outer shape is elliptical, with a region of enhanced emission on the eastern edge that is a factor of three or more greater than the rest of the nebula. There is moderate emission in [O III] and [S II]; the emission near H α is dominated by [N II], such that $F(\lambda 6548 + \lambda 6583)/F(\lambda 6563)$ probably exceeds 5. No central star is visible. (See Fig. 5.)

LMC-MG 14.—This round nebula has a bipolar core surrounding a small central zone with reduced emission, and an attached outer shell that is twice as large as the primary shell, and about one-third as bright. The [O III] emission is very strong, but the lower-ionization lines of [N II], [S II], [O I], and He I are absent. The CS is easily visible. (See Fig. 4.)

LMC-MG 16.—This bipolar nebula shows a classic butterfly shape in the broad-band, with a pinched waist of roughly 0''75, terminated by bright knots of emission. The emission in one “wing” extends at least 1''3 to the east of the very prominent CS. Much more structure is apparent in the red spectrum, where the strong [N II] emission shows what appear to be a nearly orthogonal set of loops that intersect the bright emission knots at the ends of the waist. The emission in H α and the weak [O III] lines is by comparison more uniform and compact, with no sign of loops. This is a case where the R_{phot} as measured from [O III] $\lambda 5007$ would be significantly smaller had it been determined from [N II] $\lambda 6583$, and suggests stratified ionization. There is weak emission in [S II] and possibly in [O I]. (See Fig. 4.)

LMC-MG 29.—This nebula is basically elliptical in shape, with additional structure. The broad-band image shows brightening on the ring edges to the SE and (to a lesser extent) the NW, and faint extensions to the NE and SW. A faint central star is also visible. The red spectrum reveals a striking degree of structure along the ring in the emission of [N II] which is nearly absent in the brighter emission of H α . The ring structure gives the appearance of braided strands. Emission in [O III] is very strong, though [S II] and [O I] are present but weak. (See Fig. 4.)

LMC-MG 40.—This is a very interesting elliptical nebula with a bipolar core and an attached outer shell. The pair of enhanced emission features within the core are roughly aligned with the major axis of the elliptical boundary, but are not located symmetrically along that axis. The core surface brightness is a factor of 3–4 brighter than that of the attached shell, which is also elliptical in shape but has a lower eccentricity (0.42 *vs.* 0.68). The limb of the outer shell is somewhat brightened on the eastern edge, which is suggestive of some kind of interaction with gas

just outside of the illuminated shell. The CS is easily visible in the broad-band image. (See Fig. 6.)

LMC-MG 45.—This nebula is barely resolved, but does show an elliptical shape in the emission lines. The nebular emission is very sharply peaked, and is difficult to distinguish from that of the CS. (See Fig. 6.)

LMC-MG 51.—This nebula is slightly elliptical, with a bright core surrounded by a faint, attached shell. A central emission cavity is slightly offset from the center, but overall the core is a factor of 3–5 brighter per unit area than the attached shell. The nebula is very bright in [O III] and $H\alpha$, but [N II] and the other low-ionization lines are not detected. The CS is very bright. (See Fig. 6.)

LMC-MG 60.—This nebula is slightly elliptical with a fairly uniform surface brightness, apart from a small region of enhanced brightness to the NW of the bright CS. Beyond this brighter region the nebular emission drops off abruptly along a straight line, almost as if the nebular shell had run into an invisible wall. The image was taken through the ACS/WFC F775W filter, so the emission is probably dominated by $H\alpha$ and possibly [N II]. There is a field star within the nebula, about $0''.5$ from the CS and about 2 mag fainter. (See Fig. 19.)

LMC-MG 70.—This nebula is elliptical in its outer contour, but the appearance in the light of $H\alpha$ and especially [N II] is barrel-shaped, with a distinct bipolar core. There is no CS evident in the broad-band against the bright nebular emission. (See Fig. 6.)

LMC-Mo 7.—This is a very strange, elliptical nebula with a very bright knot of emission on its southern edge. The emissions in $H\alpha$ and [O III] show something of a ring feature, though the knot is relatively brighter in $H\alpha$. There is no trace of emission in [N II] or any other low-ionization line. The CS is very bright in the broad-band. (See Fig. 6.)

LMC-Mo 17.—This is an elliptical nebula with a compact core, surrounded by a much larger shell with a surface brightness that is two to three times fainter. The nebula is distinctly brighter in the ACS/WFC F814W frame than in F555W, which may be due to stronger emission in $H\alpha$ + [N II] than in [O III]. The CS might be detected but is very faint in both frames. There are a few comparatively bright field stars within the spatial extent of the nebula, including one within $0''.9$. (See Fig. 19.)

LMC-Mo 21.—This bipolar nebula is so faint that only the ring-like waist is evident in the broad-band, along with what might be a faint CS. The emission in [N II] is much brighter than $H\alpha$, such that $F(\lambda 6548 + \lambda 6583)/F(\lambda 6563)$ probably exceeds 5. The red spectral image shows more complicated structure in the waist, with faint emission extending perpendicular to the waist at least $2''.0$. The nebula is barely detected in [O III]. (See Fig. 5.)

LMC-Mo 33.—This is an elliptical nebula with a central cavity, and relatively low average surface brightness. The outer boundary is rather sharply defined on the E and S limbs, and less so on the N and W. The $H\alpha$ emission is stronger than that from the overlapping [N II]. The [O III] emission suggests a somewhat bi-lobed ring structure. The CS is faint but apparent in the

broad-band. (See Fig. 7.)

LMC-Mo 36.—This is an elliptical nebula with fairly uniform surface brightness, apart from a fainter S limb, at the end of the major axis. The emission in [N II] has a more sharply defined edge than that in H α , and there is a suggestion of a ring or central cavity in the [N II] lines. No CS is evident in the broad-band. (See Fig. 8.)

LMC-Mo 47.—This nebula is extremely faint and the very low surface brightness makes it difficult to assess. It is probably round, and a very faint central star can be seen. It is detected in the emissions of H α and [O III], but probably not in [N II]. The derived fluxes are extremely uncertain, both because of the low intrinsic signal relative to the detector noise, and because the effects of charge transfer inefficiency are the most extreme for this case. (See Fig. 7.)

LMC-RP 265.—The extremely low surface brightness of this object and the short exposure time with the WFPC2/F606W filter makes a morphological classification difficult, but this nebula is possibly a bipolar. No CS is evident in the image. (See Fig. 19.)

LMC-Sa 104a.—This nebula is very bright, but is probably not resolved spatially. The emission lines are all extended in the dispersion direction (compared to spectra of other nebulae in this sample), however this is likely an artifact of marginally resolving the velocity profile of the gas expanding from the central source. In addition to the expected nebular lines, several other weak features are detected: some are unidentified, and some are He I or He II lines that could be nebular or stellar in origin. A deep, high-resolution spectrogram should be obtained to study the weak emission features. (See Fig. 8.)

LMC-Sa 107.—This somewhat bizarre nebula is probably bipolar, though it might be point-symmetric. It has a variety of internal structures, including an incomplete ring of emission in the center of what might be a waist, with a variety of what look to be wisps or tails of emission extending at least 1".7 away from the core, more or less symmetrically about the waist. The central cavity within the ring is broken at the N edge, and the bright CS is slightly displaced from the geometric center toward the break. The morphology is so disturbed that it is tempting to invoke jets or some other exotic shaping mechanism as an explanation. The emission in [N II] is much brighter than H α , and the [O III] emission is weak. (See Fig. 8.)

LMC-Sa 117.—This is a point-symmetric nebula, with knots of emission at each end of two separate axes that are not orthogonal, at least in projection. The knots are situated surround a cavity of emission that is slightly offset from the geometric center. The CS is easily visible. (See Fig. 8.)

LMC-Sa 121.—This is a mildly elliptical nebula with a core of relatively constant surface brightness, surrounded by a shell with a surface brightness only a factor of two lower. Two ansae extend about 0".3 to the N and S from the outer shell. The morphology is more like a ring in the light of [N II], which is no doubt due to stratification in the nebular ionization. The CS is detected but faint in the broad-band. (See Fig. 8.)

LMC-SMP 3.—This nebula is barely resolved, but is probably round. The spatial extent of the nebular emission is strongly peaked, and is difficult to distinguish from the central star on the broad-band. Continuum emission is evident in the red spectrum, but may be entirely due to nebular continuum. (See Fig. 9.)

LMC-SMP 5.—This is a mildly elliptical nebula with a single shell. The bright CS is easily detected in the broad-band, and can be seen also in the blue and red spectra. (See Fig. 9.)

LMC-SMP 6.—This elliptical nebula has a slightly bipolar core. No CS is evident in the broad-band. (See Fig. 9.)

LMC-SMP 11.—This nebula is one of the smallest known bipolar PNe in the LMC. The emission lobes are not as widely separated in the light of $H\alpha$ and [N II] (less than $0''.2$) as in [O III] (roughly $0''.35$). Interestingly, there is a detached arc of emission located $2''.3$, or 0.56 pc, from the center that extends roughly 40° from approximately S through SE. The arc is slightly more than $2''.0$ long and $0''.4$ wide, and has a surface brightness that is smaller than the main nebula by a factor of between 10 (in [O III]) to 100 (in the broadband filter). (The arc lies outside the field of view of the figure, but it would not have been visible with the chosen intensity stretch.) The emission is apparent in the light of [O III], and is just detected in the light of [N II]. This arc is reminiscent of the arc near SMP 27 described in Paper I, and later shown by Reid & Parker (2006) to be part of a large, faint halo surrounding the core nebula. SMP 11 has a fairly high aggregate expansion velocity of 122 km/s (Dopita, et al. 1988), with multiple velocity components. The CS is probably obscured by the bright nebular emission in the broad-band image. (See Fig. 9.)

LMC-SMP 14.—This bipolar nebula shows a classic butterfly shape in the broad-band, with a pinched waist of roughly $1''.6$, terminated by very bright knots of emission. The emission in [N II] is much brighter than $H\alpha$, such that $F(\lambda 6548 + \lambda 6583)/F(\lambda 6563)$ probably exceeds 5. The [N II] image shows more complicated structure in the wings, with faint emission extending perpendicular to the waist at least $1''.8$, and surrounding a central cavity of diameter roughly the size of the waist. The nebula is fairly weak in [O III]. At the center of the nebula is either a faint CS or a knot of emission. (See Fig. 10.)

LMC-SMP 29.—This nebula is somewhat irregular, but with a bipolar core. It may be the smallest recognized bipolar to date in the LMC, with significantly enhanced emission in the E lobe. The bipolarity is even more pronounced in the [N II] emission, where pairs of faint ansae can be seen extending to the S, N, and E by up to $0''.7$ from the center. No CS is evident within the bright nebulosity of the broad-band image. (See Fig. 9.)

LMC-SMP 37.—This elliptical nebula shows enhanced emission on the N rim. The nearly complete ring of emission in the light of [N II] suggests considerable stratification in the nebular ionization. No CS is detected. (See Fig. 11.)

LMC-SMP 39.—This nebula bears a striking resemblance to SMP 37 in structure, physical size, and its emission spectrum, although SMP 39 emission shows a complete, unbroken ring. No

CS is detected. (See Fig. 11.)

LMC-SMP 43.—The morphology of this round, bipolar core nebula is strikingly similar to LMC-MG 40, with its elliptical core; faint, attached shell with a brighter limb (to the E), and a relatively prominent CS. As with MG 40, SMP 43 shows some intensity enhancement near each end of the major axis of the elliptically shaped core, especially in the light of [O III]. (See Fig. 11.)

LMC-SMP 45.—This nebula is probably bipolar, with an axis of symmetry running approximately N–S. Faint emission can be seen extending at least $2''.2$ from the faint CS. The overall emission is highly irregular, though the [N II] and [S II] emission shows more wisps and a central region of reduced emission, or cavity, from low-ionization species. (See Fig. 10.)

LMC-SMP 47.—This elliptical nebula shows a faint ansa, displaced about $0''.35$ from the main nebula along the major axis to the SSE. The feature is apparent in the clear image and in the [N II] lines, but not in H α or [O III]. The nebula is very bright, with a central peak of emission in H α that is absent in [N II]. It is not clear if the CS is detected above the nebular emission, but it is saturated in the broad-band image. (See Fig. 11.)

LMC-SMP 48.—This elliptical nebula is relatively compact with emission that is fairly strongly peaked, except in the emission of [N II] and other low-ionization lines, where the flux distribution is somewhat more flat. The CS is probably not detected above the nebular emission. (See Fig. 11.)

LMC-SMP 49.—This round nebula has a central cavity of reduced emission that is evident in all the emission lines. The intensity profile falls off more slowly than most other nebulae in this sample. The enhanced emission in the NE limb might indicate an interaction with gas outside of the illuminated shell. A faint CS is detected in the broad-band image. (See Fig. 12.)

LMC-SMP 51.—This nebula is probably not resolved. The [O III] is quite strong, and [N II] is present but weak. (See Fig. 12.)

LMC-SMP 52.—This somewhat strange nebula has an elliptical outer contour, but some inner structure. In the light of the faint [N II] lines there appears to be an outer ring of emission, though in [O III] there appears to be in addition a low-contrast, inner band or waist that extends from the ESE limb to the WNW. The CS is probably not detected. (See Fig. 12.)

LMC-SMP 57.—This nebula has a round outer contour to what may be an attached outer shell. The inner shell is very elliptical, and like the bright CS, is displaced from the center of the outer shell by $0''.096$ arcsec (0.023 pc) to the ENE. Interestingly, this nebula has a plume (or jet?) of emission extending in the opposite direction (to the WSW) about $2''.6$ (0.13 pc) from the CS. Although the plume is evident in both [O III] and H α , it is about one tenth the surface brightness of the main shell and is therefore not visible in the figure. (See Fig. 12.)

LMC-SMP 61.—The emission from this elliptical nebula is relatively uniform in the center in the broad-band and the high-ionization emission lines. There is some enhanced emission on the SE and NW limbs in the light of [N II] and the other low-ionization lines, though not quite enough for

the nebula to be classified as BC. The CS is easily visible in the broad-band image. (See Fig. 12.)

LMC-SMP 62.—This elliptical nebula is unusual in that the innermost contours resemble a bar or highly oblate ellipse with the major axis oriented roughly *perpendicular* to the major axis of the outermost contours. The image in low ionization lines such as [N II] show that the central bar is terminated on each end by a small region of enhanced emission, and that the outer nebula resembles more of a box or barrel, much like a bipolar nebula. Hence, the designation as E(bc). No CS is evident within the bright nebulosity in the broad-band image. (See Fig. 13.)

LMC-SMP 63.—The emission from this elliptical nebula is strongly peaked in high ionization lines such as $H\alpha$, He I $\lambda 6678$, and [O III], but the emission in the low-ionization lines such as [N II], [S II], and [O I] shows a ring structure, with enhanced brightness on the SW edge. The CS is probably visible, in spite of the intense and strongly peaked nebular emission. (See Fig. 13.)

LMC-SMP 64.—This nebula is unresolved but very bright. The spectrum is clearly that of a PN, but the $H\alpha$ and $H\beta$ emissions are slightly broader than the other nebular lines, and the profiles are asymmetric, with enhanced emission to the red of the line centroid. There are many other faint emission lines present in the spectrogram, including He I and He II that could be of either nebular or stellar origin. A central star is visible, though saturated, in the broad-band image. A faint band structure can be seen in the G750M continuum, redward of about 6700 Å. Given the complex stellar features and the apparent brightness of the continuum, it is possible that the central ionizing source has a binary companion. A deep, high-resolution spectrum should be obtained to study the full spectrum in more detail. (See Fig. 13.)

LMC-SMP 67.—This bipolar nebula shows in the broad-band image asymmetric wings emanating from a pinched waist, surrounding a bright CS. The detailed morphology in the individual nebular lines is very similar to LMC-SMP 30 (see Paper I), in that the emission shows marked ionization stratification: i.e., the emission from [O III] tends to be more spatially confined and shows less structure than $H\alpha$, while the low ionization lines of [N II] show interlocking rings of emission surrounding a central cavity of lower emission. (See Fig. 13.)

LMC-SMP 68.—The emission in this elliptical nebula is dominated by bright knots of emission on the N, W, and S sides, though fainter knots extend slightly from the outer elliptical contour on the E and W limbs. The knots are even more sharply defined in the [O III] image, but the $H\alpha$ image shows only a moderate brightening on the W side. There is no emission in [N II] or any other low ionization line. The CS is easily visible in the broad-band image. (See Fig. 13.)

LMC-SMP 69.—This bipolar nebula has a complex morphology in detail. The most prominent feature is a central (projected) ring that defines the “waist” (as is seen in LMC-Sa 107, Mo 21, and SMP 91), with embedded bright emission knots. Extending outward at least $1''.8$ from the waist are filaments of emission. Once again, the [O III] and $H\alpha$ emission is spatially more confined than in [N II], where a central cavity is evident, suggesting some degree of ionization stratification. The emission in [N II] is much brighter than $H\alpha$, such that $F(\lambda 6548 + \lambda 6583)/F(\lambda 6563)$ probably exceeds 3. The [N II] image shows more complicated structure in the ring, and faint emission extending

away from the waist at least $2''.3$, and surrounding a central cavity of reduced emission. The CS is not evident in the broad-band image, although an apparent field star just to the S of the center might be a CS candidate. (See Fig. 14.)

LMC-SMP 73.—This elliptical nebula has a bipolar core that is evident in all emission lines, although the greater contrast between the nebular core and the lobes in the [N II] emission suggest some ionization stratification in the nebula. No CS is evident in the broad-band image. (See Fig. 14.)

LMC-SMP 74.—This elliptical nebula has very prominent bipolar characteristics, and might have been classified bipolar were it not for the nearly perfect elliptical contours at the level of a few percent of the peak emission. The central bar of emission bisects what looks to be two loops of emission along the major axis. Two bright, short arcs of emission emanate from the ends of the bar, in opposite directions and perpendicular to the bar, and then fade into the loops. The CS is marginally detected above the bright nebular emission in the broad-band image. (See Fig. 14.)

LMC-SMP 75.—This nebula is barely resolved, making the morphological classification uncertain. The low ionization lines, including [N II], have a flatter peak profile than the broad-band and [O III] images. The CS may have been detected, but is saturated in the broad-band image. (See Fig. 14.)

LMC-SMP 82.—This small, elliptical nebula has a very bright core of emission, particularly in the light of [O III]. The larger and relatively flat-topped profile in [N II] and other low-ionization lines reveals significant ionization stratification. The $H\alpha$ image shows an extension of emission to the blue of about 3.6 \AA (or if the extension is spatial, to the SSW by $0''.3$). This extension is not seen in any other detected emission line, so it is not clear whether this feature is genuine. The CS is detected in the broad-band image. (See Fig. 14.)

LMC-SMP 83.—This nebula has a very complex structure, seen in all emission lines, and is probably bipolar (though it looks somewhat point-symmetric). The pinched waist is over $2''.0$, but the largest of the four main loops of emission extends at least $3''.4$ (0.84 pc) from the center. An extensive spectroscopic study of the dynamics of this nebula was published by Pena, et al. (2004). The CS is easily detected in the broad-band image. (See Fig. 15.)

LMC-SMP 84.—This elliptical nebula has rather weak [N II], but unlike the emission in [O III] or the recombination lines, the emission is confined to narrow columns along the major axis of the nebula, indicating an interesting ionization structure. The CS is likely detected above the nebular emission in the broad-band image. (See Fig. 16.)

LMC-SMP 88.—This nebula is elliptical, and appears to have a faint extension surrounding a brighter core. The ionization appears to be somewhat stratified, judging by the larger and more pronounced ring of emission in [N II] than in [O III]. The cavity within the ring appears to be filled in $H\alpha$ with extended wings of probable stellar emission. The CS is easily visible in the broad-band image. (See Fig. 16.)

LMC-SMP 89.—This elliptical nebula shows some hint of bipolar structure in the [O III] image, with somewhat box-like inner contours. The bipolarity is less obvious in $H\alpha$, and is not present at all in the [N II] emission. The low ionization lines show an emission deficit in the center of an irregular ring, revealing some ionization stratification in the nebula. There is no CS evident in the broad-band image. In many ways this object is similar to, though smaller than, LMC-SMP 62. (See Fig. 16.)

LMC-SMP 91.—This bipolar nebula shows a classic butterfly shape in the broad-band, with a pinched waist of roughly $1''.75$ that bisects what appears to be a ring of emission in projection. The emission in [N II] is much brighter than $H\alpha$, such that $F(\lambda 6548 + \lambda 6583)/F(\lambda 6563)$ probably exceeds 5. The [N II] image shows more complicated structure in the ring, and faint emission extending away from the waist at least $2''.3$, and surrounding a central cavity of reduced emission. The cavity is far less apparent in the $H\alpha$ image. The nebula is fairly weak in [O III] but the ring is very apparent. The CS is not evident in the broad-band image. (See Fig. 15.)

LMC-SMP 92.—The emission in the E lobe of the bipolar core of this elliptical nebula is roughly 10% stronger than the W lobe in the light of $H\alpha$ and [O III], but the relative strengths are about equal in the light of [N II]. No CS is evident in the broad-band image. (See Fig. 16.)

LMC-SMP 98.—This small, round nebula has a relatively flat-topped spatial profile, though a small deficit of emission is apparent in [N II] and the other, low-ionization lines, revealing some ionization stratification within the nebula. The CS is probably not detected. (See Fig. 16.)

LMC-SMP 101.—This slightly elliptical nebula has small, faint ansae extending from the NNE and SSW limbs. The main nebula is a mostly filled shell, terminating in a ring at the outer boundary. Interestingly, the ansae are not symmetric about the center, but are displaced slightly, and lie roughly along a darker band that passes just to the E of the bright CS. The nebular features are similar in all of the emission lines, though the [O III] image shows somewhat more detailed, if disorganized, structure. (See Fig. 17.)

SMC-JD 12.—This nebula is probably bipolar, judging by the nearly orthogonal orientation between the brighter inner core and the outer regions. This nebula is very apparent in the ACS/WFC F555W band, detected but faint in the F814W band, and not detected in the F435W band. No CS is evident in the any of the broad-band images. (See Fig. 19.)

SMC-SMP 2.—This round nebula has an asymmetric brightness profile in broad-band light and in the high-ionization lines of $H\alpha$ and [O III], with higher emission on the S side. The low ionization lines such as [N II] show emission in an elliptical ring, again with somewhat brighter emission on the S edge. No CS is evident in the broad-band image. (See Fig. 18.)

SMC-SMP 3.—This elliptical nebula has a very distinct bipolar core. Interestingly, only the lobes can be seen in the [N II] emission. The CS is very apparent in the broad-band image. (See Fig. 18.)

SMC-SMP 15.—The emission from this nebula is strongly peaked in both the broad-band image, as well as the high ionization lines of $H\alpha$ and [O III]. The emission in [N II] is not as strongly peaked, and from the $\lambda 6583$ line it is possible to make an improved estimate of the nebular size, which is slightly broader than a point source. The CS might have been detected had it not saturated in the broad-band image. (See Fig. 18.)

SMC-SMP 16.—This bright, compact, slightly elliptical nebula shows strongly peaked emission in the broad-band image and the high-ionization lines of $H\alpha$ and [O III]. The emission in [N II] is somewhat more box-shaped, with a hint of enhanced brightness on the E and W limbs. The CS is probably detected in the broad-band image. (See Fig. 18.)

SMC-SMP 28.—This bright, compact nebula is round but appears to have a faint, diffuse tail of emission extending about $0''.9$ to the NW from the central star. No G750M spectrum is available. (See Fig. 18.)

4. Discussion

4.1. Broad Characteristics

As discussed in §1, there are now 114 PNe in the LMC and 35 PNe in the SMC for which *HST* images are known to exist. Owing to the nature of the surveys, these samples are heavily weighted toward the brighter nebulae. This is illustrated in Figure 20, which shows the distribution of all MCPN with measured fluxes in [O III] $\lambda 5007$; objects that have also been imaged with *HST* are indicated in the shaded portions of the histograms. The markedly different relative numbers of known, faint PNe between the LMC and the SMC is almost certainly due to the superior completeness of the SMC sample (Jacoby & De Marco 2002). Of all confirmed LMC PNe, only about 40% have published absolute fluxes in [O III] $\lambda 5007$; in the SMC the fraction is closer to 70%. More data for the LMC should be available once ongoing surveys are published in full (e.g. Reid & Parker 2006). Jacoby & De Marco (2002) published a uniform and deep survey of a significant portion of the SMC, so that this flux-complete sample can be studied in considerable detail.

The bulk of MCPNe in the *HST* samples are small, with a median photometric radius of 0.10 pc in the LMC and 0.08 pc in the SMC, as shown in Figure 21. Interestingly, there is only a rough correlation between the magnitude in [O III] $\lambda 5007$ (m_{5007} , following Ciardullo, et al. 1989) and R_{phot} , in the sense that fainter PNe tend to be larger. As illustrated in Figure 22, successive bins in the [O III] planetary nebula luminosity function (PNLF) sample a wide range of nebular sizes and morphological types, except for the brightest two magnitude bins where the PNe are typically small and bipolar nebulae are significantly under-represented. Although this *HST* sample is seriously incomplete at faint flux levels, the relative number of bipolars is much larger for nebulae fainter than about 2 mag below the brightest. We speculate that the robustness of the PNLF across galaxy type may be in part due to the heterogeneity of nebular sizes, types,

and chemical enrichments (see below) within all but the brightest one or two magnitude bins. For PNe within one magnitude of the brightest it is interesting to note that all are well resolved, and the median radius of ~ 0.06 pc suggests that most MCPNe do not attain their maximum [O III] brightness for some time after the material in the main shell is ejected by the CS. These properties, and the presence of only one bipolar PN (in the LMC) among these nebulae, suggests that few if any of the most luminous MCPNe are composed of a post-asymptotic giant branch star and a close accreting white dwarf companion, as asserted by Soker (2006). In this discussion of the PNLF, no correction has been applied for the generally modest amount of extinction, which is usually attributed to foreground dust. The median value for c , the logarithmic extinction at $H\beta$, is only 0.19 for the LMC sample and 0.10 for the SMC. The amount of optical extinction does not appear to correlate with morphological type or size.

4.2. Morphology and Evolution

Paper I presented a preliminary discussion of the decline in nebular surface brightness with photometric radius. The discussion focussed on the possibility of an evolution in nebular morphological type with age, and suggested that understanding the complexity of the co-evolution in the nebula and its central star is a prerequisite for fully understanding the diagram. We revisit this plot in Figure 23, but update it to show the extinction-corrected, average surface brightness (in $\text{erg cm}^{-2} \text{s}^{-1} \text{arcsec}^{-2}$) as a function of the physical size of the ionized shell (in pc) for all LMC and SMC PNe in the *HST* sample. To compute the average surface brightness we divided our [O III] $\lambda 5007$ flux, corrected for extinction (using our measurements of the Balmer decrement where possible: see § 2), by the area of a circle with radius equal to our photometric radius. The morphological types are indicated symbolically. The trend of the data along R^{-3} is quite apparent, as are the similarity of slope, normalization, and dispersion about the trend line (~ 0.75 dex) for both LMC and SMC PNe. It is remarkable that the surface brightnesses of a large ensemble of PNe can be so simply characterized. Renzini (1981) predicted a rather different form for the decline of PN surface brightness with radius. Based on the simple argument that for low density gas the volume emissivity is proportional to the product of the densities of electrons and ions, he argued that the volume emissivity declines as R^{-6} for an expanding nebula of fixed mass, so the average surface brightness of the projected nebula should decline as R^{-5} . Real nebulae are much more complex than this however, and other important factors can have a large impact on the evolution of the emissivity. These factors include compression of the gas as the fast CS wind impinges on the inner boundary of the main shell, the weak shock associated with the passage of an ionization front through neutral gas, and the progressive ionization of greater amounts of the surrounding neutral gas etc. (e.g., Villaver, Manchado & Garcia-Segura 2002; Perinotto, et al. 2004). It is important to note that, for nebulae with high optical depth, it is the radius of the O^{2+} zone, not the radius of the mass-bounded shell, that is being measured. Even for optically thin nebulae, R_{phot} would be defined more by the details of the density profile than by some physical boundary, and in any case it is not necessarily linearly related to the kinematical age of the nebula. Thus the surface

brightness relation may be more closely connected to characteristics of the evolution of the PN ionization than to the expansion of the shell per se.

In spite of the simplicity of the surface brightness relation, it is probably not correct to conclude that the trajectory of an individual PN is at all times parallel to the trend line. Several of the nebulae in Fig. 23 lie significantly below the trend, possibly indicating a relatively low ionization parameter. Many of these nebulae, particularly those with radii larger than about $\log R_{phot} = -0.7$, are bipolar. PN evolutionary models by Villaver, Manchado & Garcia-Segura (2002) and Perinotto, et al. (2004) predict that the most massive CSs (which have also lost the most mass on the AGB) will never fully ionize their surrounding gas shells, and the PN will never become optically thin because the CS evolves so quickly to low luminosity. Exactly when during its evolution a PN becomes optically thin depends on a number of factors, and it has a significant bearing on its detectability.

Further insight into the optical depth of PNe in this sample can be drawn from Figure 24, where the electron density is plotted against R_{phot} . For this plot we have derived nebular densities from the ratio of the [S II] $\lambda 6723$ doublets presented in this paper, and in Papers II and III when available, assuming an electron temperature of 10,000 K. Other densities were taken from Meatheringham & Dopita (1991a,b): from [S II] where possible and from [O II] $\lambda 3727$ if not. Densities for a few additional objects were derived from our own unpublished, ground-based optical spectra. Basic density information is available for most, but not all nebulae in this study; there is clearly a need for additional, deep spectroscopy for PNe in the Magellanic Clouds. It should be noted that densities larger than $\log N_e$ of 3.7 are less accurate, as this is well above the critical densities for the [S II] $\lambda\lambda 6716, 6731$ lines. The figure shows a very clear decline in density with increasing radius, roughly following a R^{-3} power law. However, for radii larger than $\log R_{phot} \sim -0.7$ there are many nebulae, all of which are bipolar (or similar morphology), that lie substantially above the trend defined by the smaller ionized shells. Indeed, nearly all of the bipolar nebulae have higher density at a given radius than those of other morphological types, and a few of them also lie substantially below the surface brightness trend line in Fig. 23 for $\log R_{phot} > -0.7$.

One might naively expect that the density of an individual nebula with constant ionized mass would decline as R^{-3} as the shell expands, but as mentioned above real nebulae are more complex. For instance, the effects of compression on the inner PN boundary by the fast wind and radiation from the CS would affect the trajectory, as would the initial density contrast between equatorial and polar regions of the proto-PN (Zhang & Kwok 1998) when the PN shell was formed. However, the mean density as measured by the [S II] lines may not be representative of all the gas. That is, the [S II] emissivities will be strongest near the critical density ($1.4\text{--}3.6 \times 10^3 \text{ cm}^{-3}$), so that the measured density will to some degree be intensity weighted, and will depend upon the details of the ionization in the region where density can be measured with S^+ . But the remarkable appearance of many relatively dense nebulae beyond $\log R_{phot} > -0.7$, some of which have modest ionized mass ($\lesssim 0.2M_\odot$), suggests that additional effects are in play, at least for bipolars. For nebulae with high optical depth, where the ionization front has not yet progressed through the entire extent of the

nebular gas, S^+ is most likely to be detected close to the ionization front (owing to its low ionization potential), and therefore in a region of elevated density. For these reasons one might expect to measure high [S II] density throughout most of the life of PNe with the most massive progenitor stars (i.e., those that never fully ionize the surrounding nebulae). Thus, it seems plausible that nebulae which remain optically thick would tend to lie above the R^{-3} trend even at large radius. In short, we believe the broad properties of bipolar PNe presented here: surface brightnesses that lie on or below the R^{-3} trend line, unusually high measured density at large radii, sometimes modest ionized mass, and their correlation (at least in the Galaxy) with the most massive PN progenitors provide support for the prediction that the most massive CSs remain optically thick throughout the PN phase. Note that conclusions such as these would not be possible from a sample of PNe for which the individual distances are not known accurately, as is typical of current Galactic samples.

4.3. Morphology and Chemical Enrichment

Chemical enrichments in PNe, primarily in N and He, have been studied for decades, and their connection to more massive progenitors is perhaps most widely expressed as the Peimbert Type I class (Peimbert 1978). The association of bipolar morphology in Galactic PNe with Type I characteristics was first studied in detail by Peimbert & Torres-Peimbert (1983) and Kaler (1983); Kaler noted that a disproportionate number of B nebulae had high values of N/O and elevated He/H, compared to nebulae with other morphologies. These findings lent support to the connection between B nebulae and more massive progenitors that experience hot-bottom burning, where C is largely converted to N and dredged-up in the progenitor AGB star prior to the ejection of the main PN shell. Stanghellini, et al. (2000) studied the chemical enrichments in LMC PNe with known morphologies, and showed that bipolar and bipolar core morphology was correlated with elevated N and depressed C abundances outside of the Galactic context.

With our greatly enlarged sample of MCPN with known morphologies, plus measurements of the nebular [N II] line fluxes, we can gain additional insight into the connection between morphology and chemical enhancements. Figure 25 shows a cumulative histogram of the ratio of the fluxes in the [N II] $\lambda\lambda 6548 + 6583$ lines to that for $H\alpha$ (hereafter, $N2/H\alpha$) for four morphological types: R, E, BC, and B. The figure includes data for both LMC and SMC PNe, though if plotted separately the differences would be masked by small number statistics, since the SMC has fewer nebulae with known morphology and a lower fraction of bipolars. The [N II] fluxes are from this paper and from Papers II and III where available, or from Meatheringham & Dopita (1991a,b). The plot shows that almost all R nebulae have $N2/H\alpha < 0.25$, and for all nebulae except one the ratio is less than 0.75. (The one exceptional R nebula is barely resolved, and the R classification is uncertain.) The histograms for the E and BC nebulae are nearly indistinguishable. Like the R nebulae about 20% have $N2/H\alpha < 0.05$, but from there the curves rise more slowly: about 20% of the nebulae have $N2/H\alpha > 1.0$, and for 10% of the nebulae the ratio exceeds 1.5. But the most striking feature of the plot is the histogram for B nebulae, where none have a ratio near zero, and only 25% have

$N2/H\alpha < 1.0$. Indeed, most B nebulae have $N2/H\alpha > 3.0$. Although the $N2/H\alpha$ is only a proxy for N abundance, Figure 26 shows that it is highly useful as a simple spectral indicator. A full abundance analysis of this MCPN sample is beyond the scope of this paper, but for the present purpose, nebulae with $N2/H\alpha > 1$ (the bulk of the B nebulae) almost certainly have an elevated N abundance. Thus, Fig. 25 provides perhaps the clearest evidence yet of the remarkable difference in chemical enhancements between PN morphological types.

5. Conclusions and Future Work

We have presented images and slitless spectra of a final survey with STIS of MCPN, which when combined with prior work with *HST*, previous surveys that we have carried out, and with a few other, mostly serendipitous observations in the *HST* archive, yields the largest sample of resolved extragalactic PNe to date. The broad properties of the MCPN were described, as were the limits to our understanding that cannot be addressed further without high-resolution images of flux-complete samples. This paper also draws some important conclusions about the effects of optical depth in PNe, and sets the stage for future observations and modelling that will further our understanding of the evolution of planetary nebulae and their central stars. An analysis of the properties of the central stars is the subject of another paper (Villaver, Stanghellini & Shaw 2006). There are a number of PNe in this sample for which detailed spectra are missing or incomplete. We have obtained spectra for some of them, from which we will derive essential physical information (such as densities), as well as chemical abundances. More deep, high-resolution images of PNe will be required in both the LMC and SMC to establish a large and complete sample to a photometric depth that is comparable to those of modern surveys (i.e., at least 6 mag of the [O III] luminosity function), so that more firm conclusions can be drawn about the range of morphological, physical, and chemical properties of PNe.

We are grateful for the assistance of the very capable STScI staff in the preparation of this very extensive observing program, and to D. Saga for the preparation of the images of the nebulae. We thank Drs. B. Balick and J. C. Blades for their participation in the observing program. We are also grateful for many careful comments from the referee which helped to improve the presentation. Support for this work was provided by NASA through grants GO-09077 and GO-10251 from Space Telescope Science Institute, which is operated by the Association of Universities for Research in Astronomy, Incorporated, under NASA contract NAS5-26555.

REFERENCES

- Alves, D. R. et al. 1997, in IAU Symp. 180, Planetary Nebulae, ed. H. J. Habing & H. Lamers (Dordrecht: Kluwer), 468
- Blades, J. C., et al. 1992, ApJ, 398, L44
- Bohlin, R. C., & Goudfrooij, P. 2003, STIS Instrument Science Report 2003–03R (Baltimore: ST ScI)
- Boroson, T., & Liebert, J. 1989, ApJ, 339, 844
- Ciardullo, R., Jacoby, G. H., Ford, H. C., & Neill, J. D. 1989, ApJ, 339, 53
- Dopita, M. A., Meatheringham, S. A., Webster, B. L., & Ford, H. C. 1988, ApJ, 327, 639
- Dopita, M. A., et al. 1996, ApJ, 460, 320
- Hodge, P. E., et al. 1998a, STIS Instrument Science Report 98–10 (Baltimore: ST ScI)
- Hodge, P. E., et al. 1998b, STIS Instrument Science Report 98–26 (Baltimore: ST ScI)
- Herald, J. E., & Bianchi, L. 2004, ApJ, 611, 294
- Jacoby, G. H. 1980, ApJS, 56, 1
- Jacoby, G. H., & De Marco, O. 2002, AJ, 123, 269
- Jacoby, G. H., & Kaler, J. B. 1993, ApJ, 417, 209
- Jacoby, G. H., Walker, & Ciardullo, R. 1990, ApJ, 365, 477
- Kaler, J. B. 1983, ApJ, 271, 188
- Kimble, R. A., et al. 1998, ApJ, 492, L83
- Leisy, P., & Dennefeld, M. 1996, in IAU Symp. 155, Planetary Nebulae, ed. R. Weinberger & A. Acker (Dordrecht: Kluwer), 433
- McGrath, M. A., Busko, I., & Hodge, P. E. 1999, STIS Instrument Science Rep. 99–03 (Baltimore: ST ScI)
- Meatheringham, S. J., & Dopita, M. A. 1991a, ApJ, 75, 407
- Meatheringham, S. J., & Dopita, M. A. 1991b, ApJ, 76, 1085
- Meyssonier, N. 1995, A&AS, 110, 545
- Morgan, D. H. 1994, A&AS, 103, 235

- Morgan, D. H., & Good, A. R. 1992, *A&AS*, 92, 571
- Peimbert, M. 1978, in *IAU Symp. 76, Planetary Nebulae Observations and Theory*, ed. Y. Terzian (Dordrecht: Reidel), 215
- Peimbert, M., and Torres-Peimbert, S. 1983, in *IAU Symp. 103, Planetary Nebulae*, ed. D. R. Flower (Dordrecht: Reidel), 233
- Pena, M., Hamann, W.-R., Ruiz, M. T., Peimbert, A., & Peimbert, M. 2004, *A&A*, 419, 583
- Perinotto, M., Schönberner, D., Steffen, M., & Calonaci, C. 2004, *A&A*, 414, 993
- Plait, P., & Gull, T. R. 1999, *PASP*, 111, 679
- Reid, W. A., & Parker, Q. A. 2006, *MNRAS*, 365, 401
- Renzini, A. 1981, in *Physical Processes in Red Giants*, ed. D. R. Flower (Dordrecht: Reidel), 431
- Sanduleak, N. 1984, in *IAU Symp. 108, Structure and Evolution of the Magellanic Clouds*, ed. S. van den Bergh & K. S. de Boer (Dordrecht: Reidel), 231
- Sanduleak, N., MacConnell, D. J., & Phillip, A. G. D. 1978, *PASP*, 90, 621
- Shaw, R. A., Stanghellini, L., Mutchler, M., Balick, B., & Blades, J. C. 2001, *ApJ*, 548, 727 (Paper I)
- Soker, N. 2006, *ApJ*, 640, 966
- Stanghellini, L., Blades, J. C., Osmer, S. J., Barlow, M. J., & Liu, X.-W. 1999, *ApJ*, 510, 687
- Stanghellini, L., Shaw, R. A., Balick, B., & Blades, J. C. 2000, *ApJ*, 534, L167
- Stanghellini, L., Shaw, R. A., Mutchler, M., Palen, S., Balick, B., & Blades, J. C. 2002, *ApJ*, 575, 178 (Paper II)
- Stanghellini, L., Shaw, R. A., Balick, B., Mutchler, M., Blades, J. C., & Villaver, E. 2003, *ApJ*, 596, 997 (Paper III)
- Stasinska, G., Richer, M. G., & Mc Call, M. L. 1998, *A&A*, 336, 667
- Stys, D., Bohlin, R. C., & Goudfrooij, P. 2004, *STIS Instrument Science Report 2004–04* (Baltimore: ST ScI)
- Vassiliadis, E. 1996, *ApJ*, 465, 748
- Vassiliadis, E., Dopita, M. A., Morgan, D. H., & Bell, F. 1992, *ApJS*, 83, 87
- Vassiliadis, E., Dopita, M. A., Meatheringham, S. J., Bohlin, R. C., Ford, H. C., Harrington, J. P., Wood, P. R., Stecher, T. P., & Maran, S.-P. 1998, *ApJ*, 503, 253

- Villaver, E., Manchado, A., & Garcia-Segura, G. 2002, ApJ, 581, 1204
- Villaver, E., Stanghellini, L., & Shaw, R. A. 2003, ApJ, 597, 298
- Villaver, E., Stanghellini, L., & Shaw, R. A. 2004, ApJ, 614, 716
- Villaver, E., Stanghellini, L., & Shaw, R. A. 2006, ApJ, submitted
- Webster, B. L. 1976, MNRAS, 174, 157
- Wood, P., et al. 1987, ApJ, 320, 178
- Woodgate, B. E., et al. 1998, PASP, 110, 1183
- Zhang, C. Y., & Kwok, S. 1998, ApJS, 117, 341

Table 1. HST Imaging Programs that Include Magellanic Cloud PNe

HST Program	PI	Instrument	Galaxy	No. Targets ^a	Reference Keys
1046	Blades, J. C.	WFPC	LMC	3	1
1266	Blades, J. C.	FOC	LMC	2	1
			SMC	2	
2266	Dopita, M.	WFPC	LMC	11	2
			SMC	4	
4075	Blades, J. C.	FOC	LMC	5	5, 7, 8
			SMC	3	
4821	Blades, J. C.	FOC	LMC	3	5, 8
			SMC	3	
4940	Blades, J. C.	FOC	LMC	5	5, 8
			SMC	1	
5185	Blades, J. C.	FOC	LMC	3	5, 8
6407	Dopita, M.	WFPC2	LMC	12	4
7303	Hamann, W.-R.	STIS:S ^b	LMC	1	10
7783	Baum, S.	STIS:I	LMC	1 ^c	3
8271	Stangellini, L.	STIS:I,S	LMC	29	4
8059	Casertano, S.	WFPC2	LMC	1 ^c	...
8663	Stangellini, L.	STIS:I,S	SMC	27	6
8702	Shaw, R.	WFPC2	SMC	13	9
9077	Shaw, R.	STIS:I,S	LMC	54	11
9285	Baum, S.	STIS:I	LMC	1 ^c	...
9584	Sparks, W.	ACS:I	LMC	1 ^c	...
9891	Gilmore, G.	ACS:I	LMC	1 ^c	...
10126	Olszewski, E.	ACS:I	SMC	1 ^c	...
10251	Shaw, R.	STIS:I,S	SMC	5	11

References. — (1)Blades, et al. (1992), (2)Dopita, et al. (1996); (3)Plait & Gull (1999); (4)Shaw et al. (2001); (5)Stangellini, et al. (1999); (6)Stangellini, et al. (2003); (7)Vassiliadis (1996); (8)Vassiliadis, et al. (1998); (9)Villaver, Stangellini & Shaw (2003); (10)Herald & Bianchi (2004); (11)this paper .

^aSome PNe were observed in multiple programs.

^bUncalibrated target acquisition image, to support spectroscopy.

^cSerendipitous discovery in pure parallel program image.

Table 2. Observing Log

Nebula	Date	Dataset	Disperser	T_{Exp} (s)	N_{Exp}
LMC Nebulae					
LMC–J 5	2001 Oct 10	O6EL02010	MIRVIS	120	2
		O6EL02020	G750M	330	2
		O6EL02030	G430M	660	2
LMC–J 33	2002 Jan 22	O6EL0L010	MIRVIS	300	2
		O6EL0L020	G750M	1500	2
		O6EL0L030	G430M	600	2
LMC–MG 4	2002 Apr 13	O6EL0S010	MIRVIS	120	2
		O6EL0S020	G750M	300	2
		O6EL0S030	G750M	1200	2
		O6EL0S040	G430M	900	2
LMC–MG 14	2002 Apr 30	O6EL12010	MIRVIS	120	2
		O6EL12020	G750M	480	2
		O6EL12030	G430M	600	2
LMC–MG 16	2002 Feb 02	O6EL14010	MIRVIS	120	2
		O6EL14020	G750M	300	2
		O6EL14030	G750M	1200	2
		O6EL14040	G430M	600	2
LMC–MG 29	2002 Jan 29	O6EL1H010	MIRVIS	120	2
		O6EL1H020	G750M	1500	2
		O6EL1H030	G430M	600	2
LMC–MG 40	2001 Aug 14	O6EL1S010	MIRVIS	120	2
		O6EL1S020	G750M	180	2
		O6EL1S030	G430M	1000	2
LMC–MG 45	2001 Aug 19	O6EL1X010	MIRVIS	120	2
		O6EL1X020	G750M	300	2
		O6EL1X030	G750M	1200	2
		O6EL1X040	G430M	600	2
LMC–MG 51	2001 Dec 10	O6EL23010	MIRVIS	120	2
		O6EL23020	G750M	300	2
		O6EL23030	G750M	1200	2
		O6EL23040	G430M	600	2
LMC–MG 70	2001 Aug 30	O6EL2M010	MIRVIS	120	2
		O6EL2M020	G750M	300	2
		O6EL2M030	G750M	1200	2
		O6EL2M040	G430M	600	2
LMC–Mo 7	2002 Feb 03	O6EL39010	MIRVIS	120	2
		O6EL39020	G750M	300	2
		O6EL39030	G750M	1200	2
		O6EL39040	G430M	600	2
LMC–Mo 21	2002 May 24	O6EL3N010	MIRVIS	120	2
		O6EL3N020	G750M	300	2
		O6EL3N030	G750M	1200	2
		O6EL3N040	G430M	600	2

Table 2—Continued

Nebula	Date	Dataset	Disperser	T_{Exp} (s)	N_{Exp}
LMC–Mo 33	2002 Feb 28	O6EL3Z010	MIRVIS	300	2
		O6EL3Z020	G750M	1620	2
		O6EL3Z030	G430M	480	2
LMC–Mo 36	2001 Dec 11	O6EL42010	MIRVIS	120	2
		O6EL42020	G750M	300	2
		O6EL42030	G750M	1200	2
LMC–Mo 47	2001 Aug 18	O6EL42040	G430M	600	2
		O6EL4D010	MIRVIS	120	2
		O6EL4D020	G750M	300	2
LMC–Sa 104a	2002 Jun 29	O6EL4D030	G750M	1200	2
		O6EL4D040	G430M	600	2
		O6EL4M010	MIRVIS	120	2
LMC–Sa 107	2002 May 18	O6EL4M020	G750M	300	2
		O6EL4M030	G750M	1200	2
		O6EL4M040	G430M	600	2
LMC–Sa 117	2001 Aug 15	O6EL4P010	MIRVIS	120	2
		O6EL4P020	G750M	640	2
		O6EL4P030	G430M	340	2
LMC–Sa 121	2001 Aug 21	O6EL4R010	MIRVIS	300	2
		O6EL4R020	G750M	820	2
		O6EL4R030	G430M	640	2
LMC–SMP 3	2002 Apr 15	O6EL4T010	MIRVIS	300	2
		O6EL4T020	G750M	1500	2
		O6EL4T030	G430M	600	2
LMC–SMP 5	2001 Sep 05	O6EL4Y010	MIRVIS	120	2
		O6EL4Y020	G750M	14	2
		O6EL4Y030	G750M	70	2
		O6EL4Y040	G750M	280	2
		O6EL4Y050	G430M	60	2
LMC–SMP 6	2001 Aug 18	O6EL4YGMQ	MIRVIS	15	1
		O6EL4Z010	MIRVIS	120	2
		O6EL4Z020	G750M	120	2
		O6EL4Z030	G430M	300	2
LMC–SMP 11	2002 Jun 06	O6EL4ZOJQ	G750M	600	1
		O6EL50010	MIRVIS	120	2
		O6EL50020	G750M	30	2
		O6EL50XBQ	MIRVIS	15	1
		O6EL50XCQ	G750M	1	1
LMC–SMP 14	2001 Dec 09	O6EL50XDQ	G750M	7	1
		O6EL50XGQ	G430M	2	1
		O6EL52010	MIRVIS	300	2
		O6EL52020	G750M	450	2
LMC–SMP 14	2001 Dec 09	O6EL52030	G430M	900	2
		O6EL54010	MIRVIS	300	2
		O6EL54020	G750M	1500	2
		O6EL54030	G430M	600	2

Table 2—Continued

Nebula	Date	Dataset	Disperser	T_{Exp} (s)	N_{Exp}
LMC–SMP 29	2002 May 31	O6EL5A010	MIRVIS	120	2
		O6EL5A020	G750M	150	2
		O6EL5A030	G430M	210	2
LMC–SMP 37	2001 Sep 03	O6EL5C010	MIRVIS	120	2
		O6EL5C020	G750M	180	2
		O6EL5C030	G430M	260	2
LMC–SMP 39	2002 Apr 19	O6EL5D010	MIRVIS	120	2
		O6EL5D020	G750M	480	2
		O6EL5D030	G430M	200	2
LMC–SMP 43	2001 Dec 08	O6EL5E010	MIRVIS	120	2
		O6EL5E020	G750M	300	2
		O6EL5E030	G430M	450	2
LMC–SMP 45	2002 Apr 27	O6EL5G010	MIRVIS	120	2
		O6EL5G020	G750M	980	2
		O6EL5G030	G430M	320	2
LMC–SMP 47	2002 Apr 25	O6EL0G010	MIRVIS	120	2
		O6EL0G020	G750M	70	2
		O6EL0G030	G750M	330	2
		O6EL0G040	G430M	90	2
		O6EL0GUJQ	MIRVIS	15	2
LMC–SMP 48	2001 Dec 11	O6CN15010	MIRVIS	120	2
		O6CN15020	G750M	68	2
		O6CN15030	G430M	132	2
	2002 Apr 26	O6EL0I010	MIRVIS	120	2
		O6EL0I020	G750M	30	2
		O6EL0I030	G750M	150	2
		O6EL0I040	G750M	600	2
		O6EL0I050	G430M	48	2
		O6EL0IL4Q	MIRVIS	15	1
LMC–SMP 49	2001 Aug 13	O6EL5H010	MIRVIS	120	2
		O6EL5H020	G750M	700	2
		O6EL5H030	G430M	200	2
LMC–SMP 51	2001 Aug 13	O6EL5I010	MIRVIS	120	2
		O6EL5I020	G750M	300	2
		O6EL5I030	G430M	440	2
LMC–SMP 52	2002 Apr 11	O6EL0M010	MIRVIS	120	2
		O6EL0M020	G750M	36	2
		O6EL0M030	G750M	180	2
		O6EL0M040	G430M	60	2
LMC–SMP 57	2002 Jun 25	O6EL5K010	MIRVIS	300	2
		O6EL5K020	G750M	800	2
		O6EL5K030	G430M	460	2
LMC–SMP 61	2002 Apr 27	O6EL5M010	MIRVIS	120	2
		O6EL5M020	G750M	80	2
		O6EL5M030	G750M	360	2
		O6EL5M040	G430M	150	2
		O6EL5MWNQ	MIRVIS	15	1

Table 2—Continued

Nebula	Date	Dataset	Disperser	T_{Exp} (s)	N_{Exp}
LMC–SMP 62	2001 Aug 31	O6EL5N010	MIRVIS	120	2
		O6EL5N020	G750M	60	2
		O6EL5N030	G750M	300	2
		O6EL5N040	G430M	70	2
LMC–SMP 63	2002 May 02	O6EL5NUAQ	MIRVIS	15	1
		O6EL0O010	MIRVIS	120	2
		O6EL0O020	G750M	34	2
		O6EL0O030	G750M	180	2
		O6EL0O040	G430M	60	2
LMC–SMP 64	2002 May 31	O6EL0OE0Q	MIRVIS	15	2
		O6EL5O010	MIRVIS	120	2
		O6EL5O020	G750M	120	2
		O6EL5O030	G750M	480	2
LMC–SMP 67	2001 Nov 27	O6EL5O040	G430M	300	2
		O6EL5P010	MIRVIS	120	2
		O6EL5P020	G750M	180	2
		O6EL5P030	G430M	250	2
LMC–SMP 68	2002 Jan 28	O6EL5Q010	MIRVIS	120	2
		O6EL5Q020	G750M	600	2
		O6EL5Q030	G430M	300	2
LMC–SMP 69	2001 Oct 16	O6EL5R010	MIRVIS	120	2
		O6EL5R020	G750M	450	2
		O6EL5R030	G430M	360	2
LMC–SMP 73	2001 Oct 23	O6EL5U010	MIRVIS	120	2
		O6EL5U020	G750M	80	2
		O6EL5U030	G750M	360	2
		O6EL5U040	G430M	150	2
		O6EL5UIYQ	MIRVIS	15	1
LMC–SMP 74	2002 Apr 28	O6EL5V010	MIRVIS	120	2
		O6EL5V020	G750M	90	2
		O6EL5V030	G430M	150	2
		O6EL5VOKQ	MIRVIS	15	1
		O6EL5VONQ	G750M	360	1
LMC–SMP 75	2001 Aug 29	O6EL5W010	MIRVIS	120	2
		O6EL5W020	G750M	300	2
		O6EL5W030	G430M	150	2
LMC–SMP 82	2002 May 14	O6EL5X010	MIRVIS	120	2
		O6EL5X020	G750M	900	2
		O6EL5X030	G430M	440	2
LMC–SMP 83	2002 Feb 28	O6EL5Y010	MIRVIS	120	2
		O6EL5Y020	G750M	50	2
		O6EL5Y030	G750M	240	2
		O6EL5Y040	G430M	90	2
		O6EL5YP1Q	MIRVIS	15	1
LMC–SMP 84	2002 Jan 05	O6EL5Z010	MIRVIS	120	2
		O6EL5Z020	G750M	150	2
		O6EL5Z030	G430M	270	2

Table 2—Continued

Nebula	Date	Dataset	Disperser	T_{Exp} (s)	N_{Exp}
LMC–SMP 88	2001 Aug 30	O6EL62010	MIRVIS	120	2
		O6EL62020	G750M	320	2
		O6EL62030	G430M	540	2
LMC–SMP 89	2001 Aug 28	O6EL63010	MIRVIS	120	2
		O6EL63020	G750M	45	2
		O6EL63030	G750M	180	2
		O6EL63040	G430M	72	2
LMC–SMP 91	2002 Jun 30	O6EL63F3Q	MIRVIS	15	1
		O6EL65010	MIRVIS	120	2
		O6EL65020	G750M	1100	2
LMC–SMP 92	2002 Jun 10	O6EL65030	G430M	600	2
		O6EL66010	MIRVIS	120	2
		O6EL66020	G750M	74	2
LMC–SMP 98	2002 Jan 29	O6EL66030	G750M	360	2
		O6EL66040	G430M	160	2
		O6EL66MAQ	MIRVIS	15	1
		O6EL67010	MIRVIS	120	2
LMC–SMP 101	2001 Aug 17	O6EL67020	G750M	120	2
		O6EL67030	G750M	600	2
		O6EL67040	G430M	110	2
LMC–SMP 101	2001 Aug 17	O6EL68010	MIRVIS	120	2
		O6EL68020	G750M	200	2
		O6EL68030	G430M	270	2
SMC Nebulae					
SMC–SMP 2	2004 Jul 22	O8Y040010	MIRVIS	120	2
		O8Y040020	G750M	150	2
		O8Y040030	G750M	600	2
		O8Y040040	G430M	120	2
SMC–SMP 3	2004 Jul 17	O8Y041010	MIRVIS	120	2
		O8Y041020	G750M	1200	2
		O8Y041030	G430M	900	2
SMC–SMP 15	2004 Jul 13	O8Y046010	MIRVIS	120	2
		O8Y046020	G750M	60	2
		O8Y046030	G750M	240	2
SMC–SMP 16	2004 Jul 22	O8Y046040	G430M	210	2
		O8Y047010	MIRVIS	120	2
		O8Y047020	G750M	120	2
		O8Y047030	G750M	480	2
SMC–SMP 28	2004 Jul 14	O8Y047040	G430M	360	2
		O8Y052010	MIRVIS	120	2
		O8Y052020	G430M	1200	2

Table 3. Log of HST Images from Other Programs

Nebula	GO Program	Date	Dataset	Instrument/ Aperture	Filter	T_{Exp} (s)	N_{Exp}
LMC Nebulae							
LMC–MA 17	7303	1999 Jan 6	O57N01GLQ	STIS/50CCD	MIRVIS	200	1
LMC–MG 60	9584	2003 Feb 22	J8G9SDD6Q	ACS/WFC	F775W	750	1
			J8G9SDDDBQ		F775W	604	1
LMC–Mo 17	9891	2003 Oct 8	J8NE55Z9Q	ACS/WFC1	F555W	300	1
			J8NE55ZEQ		F814W	200	1
LMC–Mo 36	9285	2001 Dec 11	O6J3LGT1Q	STIS/50CCD	MIRVIS	200	1
			O6J3LGT2Q		MIRVIS	200	1
LMC–RP 265	8059	2001 Aug 17	U4W0E702B	WFPC2/WFALL	F606W	240	2
SMC Nebulae							
SMC–JD 12	10126	2004 Oct 30	J90604KSQ	ACS/WFC1	F435W	440	1
			J90604KTQ		F555W	440	1
			J90604KWQ		F555W	120	1
			J90604KXQ		F814W	440	1
			J90604L0Q		F814W	120	1

Table 4. Spectrum Extraction Parameters

Nebula	Center		
	G430M (pixel)	G750M (pixel)	Width (pixel)
LMC Nebulae			
LMC–J 5	517	514	43
LMC–J 33	496	492	33
LMC–MG 4	470	466	67
LMC–MG 14	516	512	37
LMC–MG 16	520	518	55
LMC–MG 29	491	487	49
LMC–MG 40	537	533	29
LMC–MG 45	562	558	9
LMC–MG 51	510	505	29
LMC–MG 70	509	504	25
LMC–Mo 7	495	492	21
LMC–Mo 21	523	520	83
LMC–Mo 33	501	496	83
LMC–Mo 36	494	489	19
LMC–Mo 47	515	513	69
LMC–Sa 104a	534	530	13
LMC–Sa 107	529	525	45
LMC–Sa 117	515	511	31
LMC–Sa 121	548	543	41
LMC–SMP 3	493	489	11
LMC–SMP 5	502	498	15
LMC–SMP 6	535	531	15
LMC–SMP 11	496	494	19
LMC–SMP 14	507	503	21
LMC–SMP 29	507	503	21
LMC–SMP 37	483	479	15
LMC–SMP 39	518	513	15
LMC–SMP 43	557	553	25
LMC–SMP 45	522	518	51
LMC–SMP 47	565	561	21
LMC–SMP 48	507	502	15
LMC–SMP 49	535	530	31
LMC–SMP 51	543	539	11
LMC–SMP 52	527	522	19
LMC–SMP 57	510	507	23
LMC–SMP 61	547	542	21
LMC–SMP 62	525	520	27
LMC–SMP 63	531	528	19
LMC–SMP 64	510	505	15
LMC–SMP 67	472	468	27

Table 4—Continued

Nebula	Center		Width (pixel)
	G430M (pixel)	G750M (pixel)	
LMC–SMP 68	532	538	31
LMC–SMP 69	520	516	61
LMC–SMP 73	496	492	23
LMC–SMP 74	489	484	21
LMC–SMP 75	513	509	17
LMC–SMP 82	502	499	19
LMC–SMP 83	521	517	75
LMC–SMP 84	480	476	21
LMC–SMP 88	522	518	17
LMC–SMP 89	541	536	21
LMC–SMP 91	546	542	115
LMC–SMP 92	527	523	23
LMC–SMP 98	455	451	13
LMC–SMP 101	540	536	47
SMC Nebulae			
SMC–SMP 2	514	509	20
SMC–SMP 3	518	514	20
SMC–SMP 15	495	492	14
SMC–SMP 16	546	542	15
SMC–SMP 28	462	...	13

Table 5. Relative Emission Line Intensities of Magellanic Cloud Nebulae

Nebula (1)	log F(H β) (λ 4861) (2)	c (3)	[O III] (λ 4959) (4)	[O III] (λ 5007) (5)	[O I] (λ 6300) (6)	[S III] (λ 6312) (7)	[O I] (λ 6363) (8)	[N II] (λ 6548) (9)	H α (λ 6563) (10)	[N II] (λ 6583) (11)	He I (λ 6678) (12)	[S II] (λ 6717) (13)	[S II] (λ 6731) (14)
LMC Nebulae													
LMC-J 5	-13.46 ^a	...	166.2	488.2	1298. ^{a,b}	37.0 ^c	33.2 ^c
LMC-J 33	-13.79	0.00	312.9	922.2	281.7
LMC-MG 4	-14.13 ^d	...	260.0	797.9	1975. ^{b,e}	237.9 ^f	...
LMC-MG 14	-13.58	0.0	358.3	1053.4	280.3	...	0.0	0.0	0.0
LMC-MG 16	-13.95	...	234.0	709.3	1545. ^b	124.2 ^f	...
LMC-MG 29	-13.54	0.15:	359.7	1045.2	11.2	...	3.0	44.9	320.8 ^e	134.3	...	20.6 ^f	...
LMC-MG 40	-13.68	0.17	247.4	725.6	326.9
LMC-MG 45	-13.15	0.78	477.3	1406.0	12.8	3.5	4.6	12.1	536.4	38.8	7.6	1.4	2.6
LMC-MG 51	-14.03	0.00	250.5	763.8	279.9
LMC-MG 70	-13.79	0.19	323.2	958.5	20.3	3.4	7.4	99.3	331.3	303.2	6.5	15.7	19.1
LMC-Mo 07	-14.20	0.01	193.2	569.4	286.3
LMC-Mo 21	-14.37	...	139.5	434.0	2828. ^{b,e}
LMC-Mo 33	-13.79	...	326.1	991.3	447.2 ^b	42.0 ^f	...
LMC-Mo 36	-14.26	0.29	272.7	779.5	18.9	139.4	360.4	416.5	...	56.9	55.7
LMC-Mo 47	-14.0 ^d	...	127.4	378.9	221.1 ^b
LMC-Sa 104a	-12.66	0.07	61.0	184.6	3.1	1.9	1.1	1.3	303.9	3.6	1.3	0.35	0.54
LMC-Sa 107	-13.91	0.51	282.9	1057.4	432.1	430.8	1295.5	6.4:	167.3 ^f	...
LMC-Sa 117	-13.64	0.21	217.7	643.5	338.8
LMC-Sa 121	-13.83	0.00	247.1	718.9	31.5	78.4	284.3	234.6	...	36.9 ^c	34.0 ^c
LMC-SMP 3	-12.48	0.01	134.3	395.3	1.4	0.6	0.6	2.7	286.3	8.9	4.0	0.2	0.6
LMC-SMP 5	-12.88	0.03	96.0	298.6	8.4	291.7	25.3	3.8	1.7	2.6
LMC-SMP 6	-12.89	0.69	581.4	1821.7	13.6	18.9	498.4	55.0	8.1
LMC-SMP 11	-13.94	0.31	16.0	60.7	163.6	...	53.6	99.7	366.1	315.7	...	34.6	72.3
LMC-SMP 14	-13.72	...	255.0	773.8	31.1	1675. ^{b,e}	...	2.1:	129.1 ^f	...
LMC-SMP 29	-12.74	0.21	336.5	991.7	...	5.4	9.4	142.7	337.7	437.8	3.7	14.7	26.2
LMC-SMP 37	-12.92	0.20	393.6	1169.8	11.5	3.2	3.3	74.6	334.5	237.0	2.5	7.2	12.0
LMC-SMP 39	-13.27	0.31	386.1	1164.3	20.5	2.7	7.1	49.0	367.0	149.5	3.9	16.2	27.0
LMC-SMP 43	-13.12	0.15	374.2	1116.5	320.5
LMC-SMP 45	-13.13	0.40	406.2	1219.8	4.6	36.1	393.5	105.2	4.5	44.0 ^f	...
LMC-SMP 47	-12.54	0.23	340.8	1027	12.5	4.4	4.0	99.9	343.8	307.3	3.7	5.2	10.7

Table 5—Continued

Nebula (1)	log F(H β) (λ 4861) (2)	c (3)	[O III] (λ 4959) (4)	[O III] (λ 5007) (5)	[O I] (λ 6300) (6)	[S III] (λ 6312) (7)	[O I] (λ 6363) (8)	[N II] (λ 6548) (9)	H α (λ 6563) (10)	[N II] (λ 6583) (11)	He I (λ 6678) (12)	[S II] (λ 6717) (13)	[S II] (λ 6731) (14)
LMC-SMP 48	-12.48	0.27	227.2	679.8	3.6	1.3	1.1	9.1	352.9	27.3	4.8	1.1	2.4
LMC-SMP 49	-13.21	0.11:	345.3	1031.3		15.6 ^g	4.1	50.0: ^h	310.3 ^h	141.1 ^h	2.8	32.9	34.4
LMC-SMP 51	-13.06	0.86	346.6	1044.1	4.7	2.3	1.6	6.2	568.5	21.5	7.7	0.7	1.3
LMC-SMP 52	-12.63	0.24	468.5	1440.	4.0	2.5	1.2	8.0	345.8	24.4	4.5	3.8	6.9
LMC-SMP 57	-13.61	0.19	337.2	1034.7 ⁱ	333.3 ⁱ	...	3.6:
LMC-SMP 61	-12.48	0.22	255.1	762.7	...	1.4	1.6	10.9	340.9	34.5	4.8	2.2 ^c	4.3 ^c
LMC-SMP 62	-12.30	0.07	343.6	1032.9	6.2	3.5	2.1	13.2	302.7	38.7	3.2	3.3	5.7
LMC-SMP 63	-12.46	0.14	307.3	949.3	2.9	2.1	1.2	6.2	319.3	19.0	4.5	1.3	2.4
LMC-SMP 64	-12.78	1.12	7.5	22.4	6.8	5.9	2.5	12.4	704.9	44.8	2.9	0.8	0.8
LMC-SMP 67	-12.78	0.14	101.6	304.6	1.7	1.2:	...	87.0	317.9	265.7	4.4	2.7	4.3
LMC-SMP 68	-13.17	0.00	218.8	628.7	281.3
LMC-SMP 69	-13.43	...	285.9	872.1	42.3:	...	8.9:		1509.5 ^{b,e}		...	104.9 ^f	
LMC-SMP 73	-12.55	0.17	486.5	1458.3	11.2	2.6	4.3	19.0	327.1	56.6	4.1: ^j	3.3: ^j	7.2: ^j
LMC-SMP 74	-12.64	0.09	385.6	1146.3	7.4	2.4:	2.5:	9.3	306.2	36.2	4.3	3.3	7.4
LMC-SMP 75	-12.53	0.26	339.2	979.1	4.8	1.5	1.7	8.6	350.7	26.4	5.3	1.0	2.2
LMC-SMP 82	-13.62	0.47	375.4	1156.8	14.5	8.5	5.3	125.3	417.4	372.2	9.3	15.0	23.2
LMC-SMP 83	-12.67	...	282.7	800.2		8.5 ^g	...		507.5 ^b		...	22.4 ^f	
LMC-SMP 84	-12.68	0.08	229.9	682.7	...	1.7:	...	2.7:	303.6	6.3	3.4
LMC-SMP 88	-13.44	0.58	113.5	333.0	9.8	3.5	3.7	50.0	453.8	155.2	5.8:	7.9	13.1
LMC-SMP 89	-12.61	0.31	431.7	1309.9	9.7	2.4	3.2	13.1	366.6	40.3	4.4	3.3	6.3
LMC-SMP 91	-13.59	...	282.7	852.9		48.6 ^g	14.4		1902.9 ^{b,e}		...	145.5: ^f	
LMC-SMP 92	-12.58	0.16	466.8	1386.6	...	2.7	3.8	20.4	325.4	64.1	3.5	5.3	9.4
LMC-SMP 98	-12.54	0.28	478.5	1395.5	10.3:	4.3	3.6	13.3	356.7	41.0	4.2	2.0	4.7
LMC-SMP 101	-12.93	0.08:	387.4	1138.1	4.1 ^h	303.5 ^h	11.9 ^h
SMC Nebulae													
SMC-SMP 02	-12.71	0.00	303.6	909.0	2.8	1.4	0.9	3.5	283.0	10.0	3.0	1.4	2.4
SMC-SMP 03	-13.13	0.00	272.5	816.6	...	< 1.0	< 1.0	1.1	284.0	3.3	3.8	< 1.0	< 1.0
SMC-SMP 15	-12.45	0.01	208.2	584.4	1.9	0.8	0.7	4.4	286.8	13.5	4.5	0.4	1.0
SMC-SMP 16	-12.74	0.03	57.2	165.5	1.4	0.7	0.5	11.6	291.9	35.5	3.2	1.1	2.3
SMC-SMP 28	-13.18	...	93.6	278.7

^aBulk of H⁺ emission is probably from CS (see text).

^bIntensity of the blend of H α and [N II] λ 6548,6583.

^cPartial blending of doublet [S II] λ 6716,6731.

^dExtremely weak surface brightness in this line renders flux measurement extremely uncertain.

^eIntensity of [N II] λ 6548,6583 dominates emission from H α (see text).

^fIntensity of the blended doublet [S II] λ 6716,6731.

^gIntensity of the blend of [O I] λ 6300 and [S III] λ 6312.

^hPartial blending of [N II] λ 6548 and H α .

ⁱApproximately 7% of the emission is contained in the plume (see text).

^jGreater uncertainty due to complicated stellar continuum.

Table 6. Coordinates, Dimensions, and Morphologies of Magellanic Cloud Nebulae

Nebula (1)	R.A. J(2000) (2)	Decl. (J2000) (3)	R_{phot} (arcsec) (4)	Diameter (arcsec) (5)	Morph. Class (6)	Figure (7)	Notes (8)
LMC Nebulae							
LMC–J 5	5 11 48.05	–69 23 42.2	0.67	0.97 x 1.48	E	4	Stellar emission, P-Cyg?
LMC–J 33	5 21 18.11	–69 43 01.9	0.69	1.53 x 1.79	E	4	Attached shell
LMC–MA 17	5 55 13.78	–65 28 23.5	...	0.88 x 0.67	Q	19	Jets
LMC–MG 4	4 52 44.83	–70 17 50.6	1.19	4.3 x 3.3	E?	5	Faint; could be B?
LMC–MG 14	5 04 27.67	–68 58 12.3	0.56	1.58	R(bc)	4	Attached shell
LMC–MG 16	5 06 05.22	–64 48 48.9	0.62	1.28 x 1.63	B	4	
LMC–MG 29	5 13 42.48	–68 15 17.9	1.21	1.48 x 2.30	E	4	
LMC–MG 40	5 22 35.36	–68 24 26.5	0.70	0.38 x 0.33	E(bc)	6	Attached shell
LMC–MG 45	5 26 06.45	–63 24 04.4	0.20	0.31 x 0.23	E	6	
LMC–MG 51	5 28 34.47	–70 33 01.9	0.62	1.22 x 1.43	E	6	Attached shell
LMC–MG 60	5 33 30.95	–69 08 13.6	...	1.20 x 1.15	R	19	
LMC–MG 70	5 38 12.37	–75 00 21.6	0.31	0.48 x 0.67	E(bc)	6	
LMC–Mo 7	4 49 19.86	–64 22 36.8	0.43	0.72 x 0.93	E	6	
LMC–Mo 17	5 07 35.06	–67 29 02.1	...	2.07 x 1.54	E	19	Attached shell; inner core: $0''.64 \times 0''.58$
LMC–Mo 21	5 19 04.11	–64 44 39.3	1.06	3.1 x 2.9	B	5	
LMC–Mo 33	5 32 09.75	–70 24 43.7	1.93	2.12 x 1.58	E(bc?)	7	
LMC–Mo 36	5 38 53.81	–69 57 56.0	0.34	1.14 x 0.97	E	8	
LMC–Mo 47	6 13 03.35	–65 55 09.4	1.28	3.47	R	7	v. faint
LMC–RP 265	5 37 00.7	–69 21 29.	...	4.2 x 3.4	B?	19	v. faint
LMC–Sa 104a	4 25 32.15	–66 47 18.5	...	< 0.25	...	8	Resolved velocity structure
LMC–Sa 107	5 06 43.81	–69 15 38.4	0.75	1.70 x 1.62	B?	8	Could be P?
LMC–Sa 117	5 24 56.82	–69 15 31.2	0.77	1.18 x 1.30	P	8	
LMC–Sa 121	5 30 26.20	–71 13 49.5	0.58	1.58 x 1.65	E	8	Ansa; attached shell
LMC–SMP 3	4 42 23.79	–66 13 01.0	0.15	0.26 x 0.23	R?	9	Barely resolved
LMC–SMP 5	4 48 08.62	–67 26 06.5	0.27	0.46 x 0.50	E	9	
LMC–SMP 6	4 47 38.97	–72 28 21.6	0.25	0.67 x 0.56	E(bc)	9	
LMC–SMP 11	4 51 37.69	–67 05 16.1	0.43	0.76 x 0.55	B	9	Detached arc
LMC–SMP 14	5 00 21.09	–70 58 52.3	1.33	2.41 x 1.87	B	10	
LMC–SMP 29	5 08 03.34	–68 40 16.8	0.27	0.51 x 0.47	BC	9	Irregular, B?
LMC–SMP 37	5 11 03.12	–67 47 57.6	0.25	0.50 x 0.43	E	11	
LMC–SMP 39	5 11 42.26	–68 34 59.3	0.23	0.60 x 0.55	E	11	Ring?
LMC–SMP 43	5 17 02.40	–69 07 16.1	0.55	1.11	R(bc)	11	Attached shell
LMC–SMP 45	5 19 20.75	–66 58 08.4	0.72	1.66 x 1.62	B?	10	
LMC–SMP 47	5 19 54.88	–69 31 04.3	0.25	0.45 x 0.32	E	11	J 25; ansa to SSE
LMC–SMP 48	5 20 09.66	–69 53 39.2	0.20	0.40 x 0.35	E	11	J 27
LMC–SMP 49	5 20 09.46	–70 25 38.5	0.65	1.00	R	12	
LMC–SMP 51	5 20 52.56	–70 09 36.6	12	Unresolved
LMC–SMP 52	5 21 23.75	–68 35 34.9	0.20	0.73	R	12	J 34
LMC–SMP 57	5 23 48.69	–69 12 20.9	0.43	0.93 x 0.90	R(bc)	12	Asymmetric core; attached shell; plume
LMC–SMP 61	5 24 36.37	–73 40 40.0	0.26	0.56 x 0.54	E	12	
LMC–SMP 62	5 24 55.24	–71 32 56.4	0.27	0.59 x 0.41	E(bc)	13	

Table 6—Continued

Nebula (1)	R.A. J(2000) (2)	Decl. (J2000) (3)	R_{phot} (arcsec) (4)	Diameter (arcsec) (5)	Morph. Class (6)	Figure (7)	Notes (8)
LMC–SMP 63	5 25 26.12	–68 55 55.4	0.26	0.63 x 0.57	E	13	J 39
LMC–SMP 64	5 27 35.69	–69 08 56.4	...	< 0.25	...	13	Stellar emission?
LMC–SMP 67	5 29 16.01	–67 32 48.0	0.33	0.88 x 0.61	B	13	
LMC–SMP 68	5 29 02.83	–70 19 23.8	0.71	1.33 x 0.97	E(s)	13	
LMC–SMP 69	5 29 23.31	–67 13 21.9	1.03	1.84 x 1.43	B	14	
LMC–SMP 73	5 31 22.27	–70 40 45.3	0.25	0.31 x 0.27	E(bc)	14	
LMC–SMP 74	5 33 29.51	–71 52 27.9	0.35	0.79 x 0.63	E(bc)	14	Might be B?
LMC–SMP 75	5 33 47.00	–68 36 44.0	0.20	0.33	R	14	
LMC–SMP 82	5 35 57.47	–69 58 16.6	0.20	0.31 x 0.30	E	14	
LMC–SMP 83	5 36 20.82	–67 18 07.0	1.26	3.98 x 3.63	B?	15	Could be P?
LMC–SMP 84	5 36 53.17	–71 53 39.8	0.29	0.57 x 0.48	E	16	
LMC–SMP 88	5 42 33.27	–70 29 24.2	0.36	0.61 x 0.45	E	16	
LMC–SMP 89	5 42 36.84	–70 09 32.0	0.23	0.51 x 0.45	E(bc?)	16	
LMC–SMP 91	5 45 06.02	–68 06 49.1	1.12	1.89 x 1.40	B	15	
LMC–SMP 92	5 47 04.63	–69 27 34.5	0.26	0.62 x 0.54	E(bc)	16	
LMC–SMP 98	6 17 35.59	–73 12 37.3	0.20	0.41	R	16	
LMC–SMP 101	6 23 40.24	–69 10 38.9	0.81	1.03 x 0.82	E(bc?)	17	Ansa?
SMC Nebulae							
SMC–JD 12	0 51 07.31	–73 12 04.4	...	1.15 x 1.40	B?	19	
SMC–SMP 2	0 32 38.81	–71 41 58.7	0.25	0.54	R	18	
SMC–SMP 3	0 34 21.89	–73 13 20.4	0.27	0.59 x 0.48	E(bc)	18	
SMC–SMP 15	0 51 07.45	–73 57 37.1	0.17	0.32	R	18	
SMC–SMP 16	0 51 27.08	–72 26 11.1	0.18	0.33 x 0.30	E	18	
SMC–SMP 28	1 24 12.09	–74 02 31.4	0.21	0.31	R	18	Ansa?

Figure Captions

Fig. 4.— Images (*left*), and slitless spectra in [O III] $\lambda 5007$ (*center*) and the triplet of [N II] $\lambda 6548$, H α , and [N II] $\lambda 6583$ (*right*) of the PN targets in the STIS survey. The images are $3''$ on a side with a log intensity stretch unless otherwise indicated. The LMC nebulae are, from top to bottom, J 5, J 33, MG 14 (square-root intensity scale), MG 16, and MG 29. The orientation for each image is indicated on the figure, with north lying in the direction of the arrow and east to the left.

Fig. 5.— Same as Fig. 4 for the LMC nebulae MG 4, and Mo 21, except that the images are $4'' \times 4''$.

Fig. 6.— Same as Fig. 4 for the LMC nebulae: MG 40, MG 45, MG 51, MG 70, and Mo 7.

Fig. 7.— Same as Fig. 4 for the LMC nebulae Mo 33 ($6'' \times 6''$), and Mo 47 ($4'' \times 4''$).

Fig. 8.— Same as Fig. 4 for the LMC nebulae Mo 36 (square-root intensity scale), Sa 104a, Sa 107, Sa 117, and Sa 121.

Fig. 9.— Same as Fig. 4 for the LMC nebulae SMP 3, SMP 5, SMP 6 (square-root intensity scale), SMP 11, and SMP 29.

Fig. 10.— Same as Fig. 4 for the LMC nebulae SMP 14, and SMP 45, except that the images are $4'' \times 4''$.

Fig. 11.— Same as Fig. 4 for the LMC nebulae SMP 37, SMP 39, SMP 43, SMP 47, and SMP 48.

Fig. 12.— Same as Fig. 4 for the LMC nebulae SMP 49, SMP 51, SMP 52, SMP 57, and SMP 61.

Fig. 13.— Same as Fig. 4 for the LMC nebulae SMP 62, SMP 63, SMP 64, SMP 67, and SMP 68.

Fig. 14.— Same as Fig. 4 for the LMC nebulae SMP 69, SMP 73, SMP 74, SMP 75, and SMP 82.

Fig. 15.— Same as Fig. 4 for the LMC nebulae SMP 83 ($6'' \times 6''$), and SMP 91 ($4'' \times 4''$).

Fig. 16.— Same as Fig. 4 for the LMC nebulae SMP 84, SMP 88, SMP 89, SMP 92, and SMP 98.

Fig. 17.— Same as Fig. 4 for the nebula LMC–SMP 101.

Fig. 18.— Same as Fig. 4 for the SMC nebulae SMP 02, SMP 03, SMP 15, SMP 16, and SMP 28.

Fig. 19.— PNe observed in other *HST* programs, on the same spatial scale as for Fig. 4, with a square-root intensity stretch. The nebulae and spatial extent of the images are: LMC–MA 17 ($4'' \times 4''$ with log intensity stretch), LMC–MG 60 ($4'' \times 4''$), LMC–Mo 17 ($7'' \times 6''$), LMC–RP 265 ($4'' \times 4''$), and SMC–JD 12 ($3'' \times 3''$). The orientations are indicated next to each image, with north lying in the direction of the arrow and east to the left.

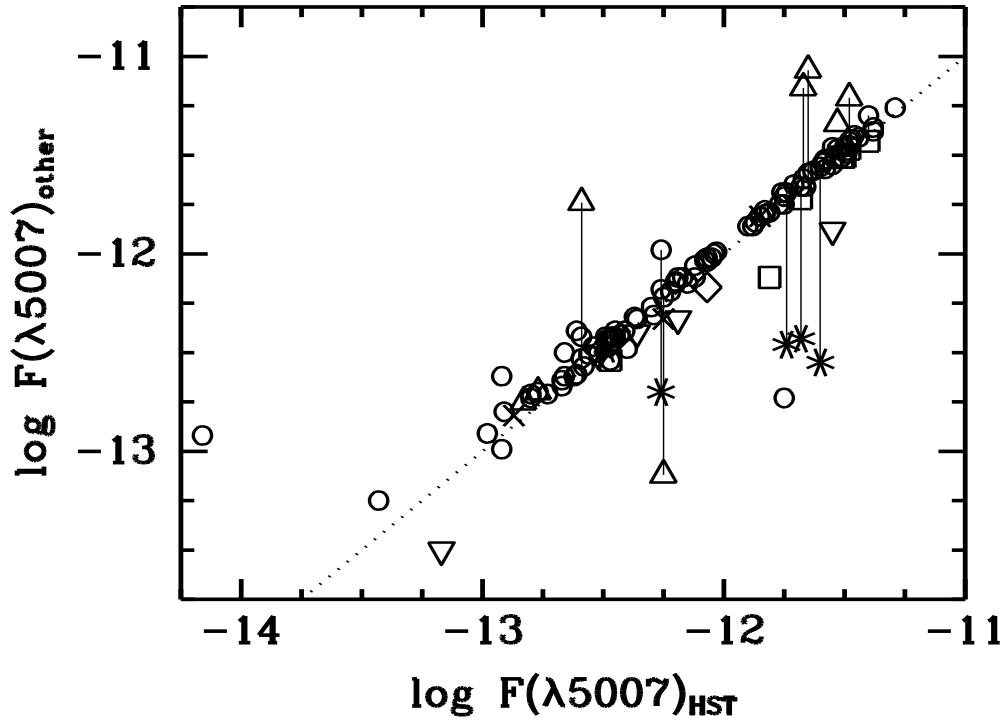


Fig. 1.— Comparison of the log flux in [O III] $\lambda 5007$ (in $\text{erg cm}^{-2} \text{s}^{-1}$) of various published values and those reported in this paper and in Papers II and III, with the 1:1 relation indicated (*dotted line*). Symbol key: Jacoby, Walker & Ciardullo (1990) (*circles*); Jacoby & Kaler (1993) (*squares*); Boroson & Liebert (1989) (*triangles*); Vassiliadis, et al. (1992) (*inverted triangles*); Wood, et al. (1987) (*diamonds*); Meyssonnier (1995) (*crosses*); Webster (1976) (*asterisks*). Examples of objects observed by more than one other investigator are connected with thin vertical lines.

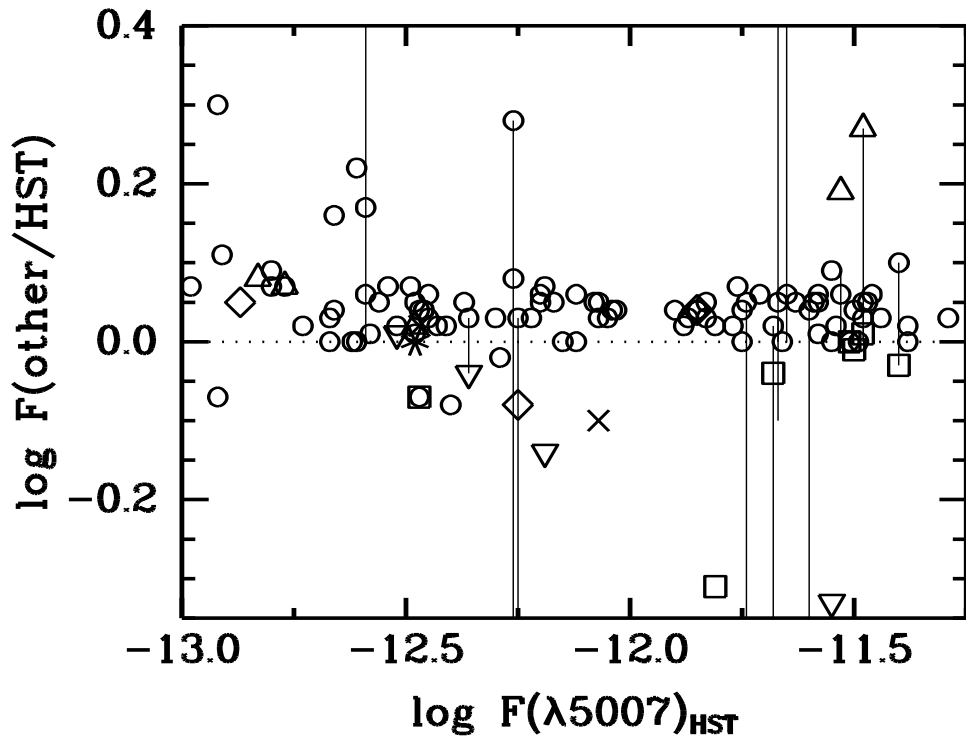


Fig. 2.— Same as Fig. 1, except the ordinate is the log of the ratio of the flux in [O III] between various published values and those reported in this paper and in Papers II and III. Symbols are as in Fig 1.

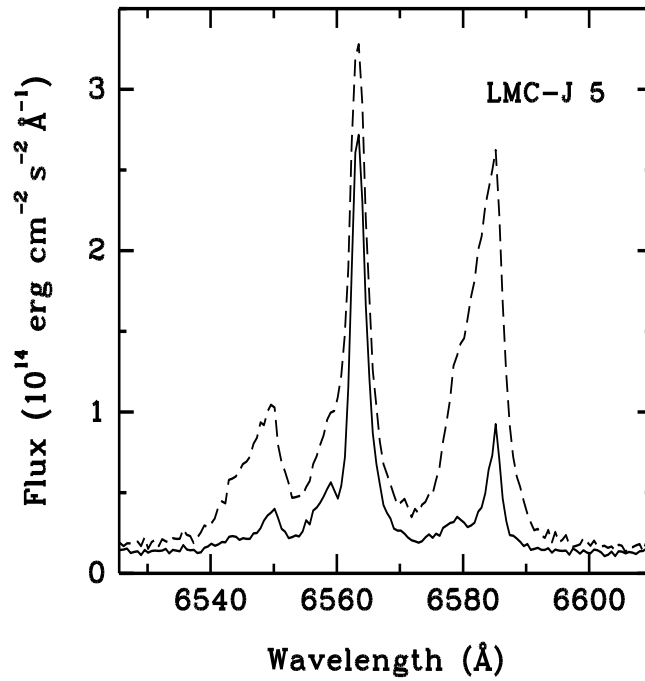


Fig. 3.— Spectrum of LMC-J 5, comparing the emission of $\text{H}\alpha$ and $[\text{N II}] \lambda\lambda 6548, 6583$ from the nebula plus star (*dashed*) to that of the star (*solid*) from a 3 pixel virtual extraction slit.

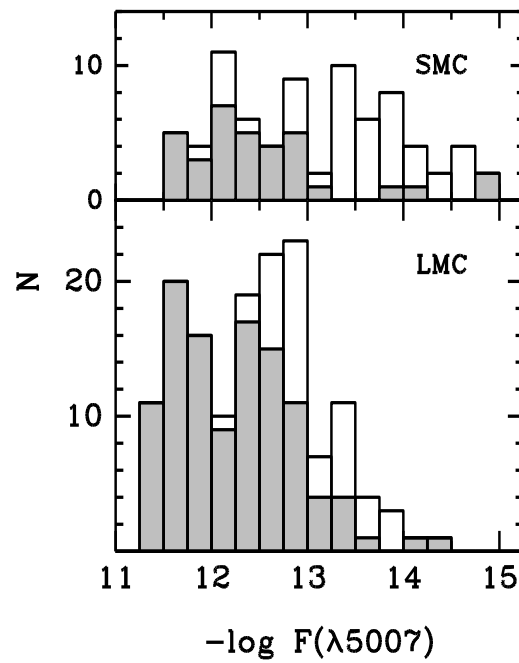


Fig. 20.— Histogram of PN with published fluxes in [O III] $\lambda 5007$ ($\text{erg cm}^{-2} \text{s}^{-1}$) for the SMC (*upper*) and LMC (*lower*). Nebulae that have been observed with *HST* are indicated (*shaded*) in each histogram.

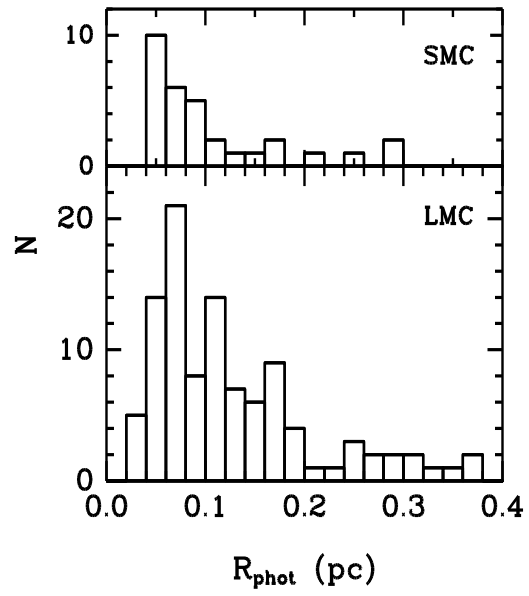


Fig. 21.— Histogram of nebular photometric radii for the SMC (*upper*) and LMC (*lower*).

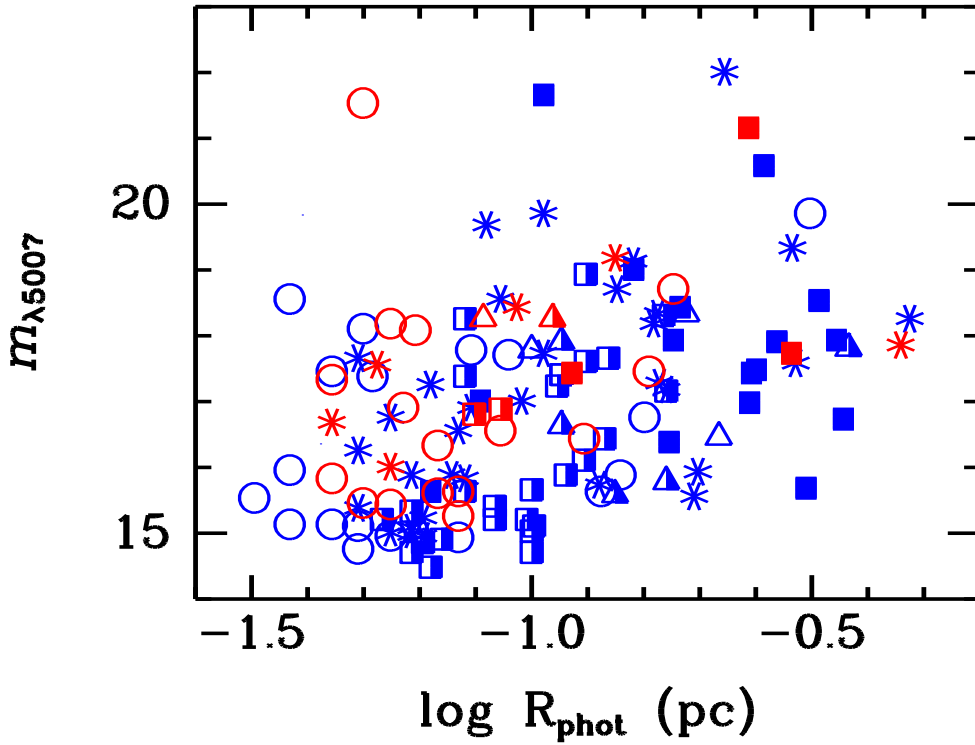


Fig. 22.— Variation of the flux in [O III] $\lambda 5007$, uncorrected for interstellar extinction and expressed in magnitudes ($m_{5007} = -2.5 \log F_{5007} - 13.74$), with photometric radius for the LMC and SMC nebulae. Symbols indicate morphological type: round (*circles*), elliptical (*asterisks*), quadrupolar (*half-filled triangles*), bipolar (*filled squares*), bipolar core (*half-filled squares*), and point-symmetric (*open triangles*). The electronic version of this paper shows LMC PNe in blue symbols, and SMC PNe in red.

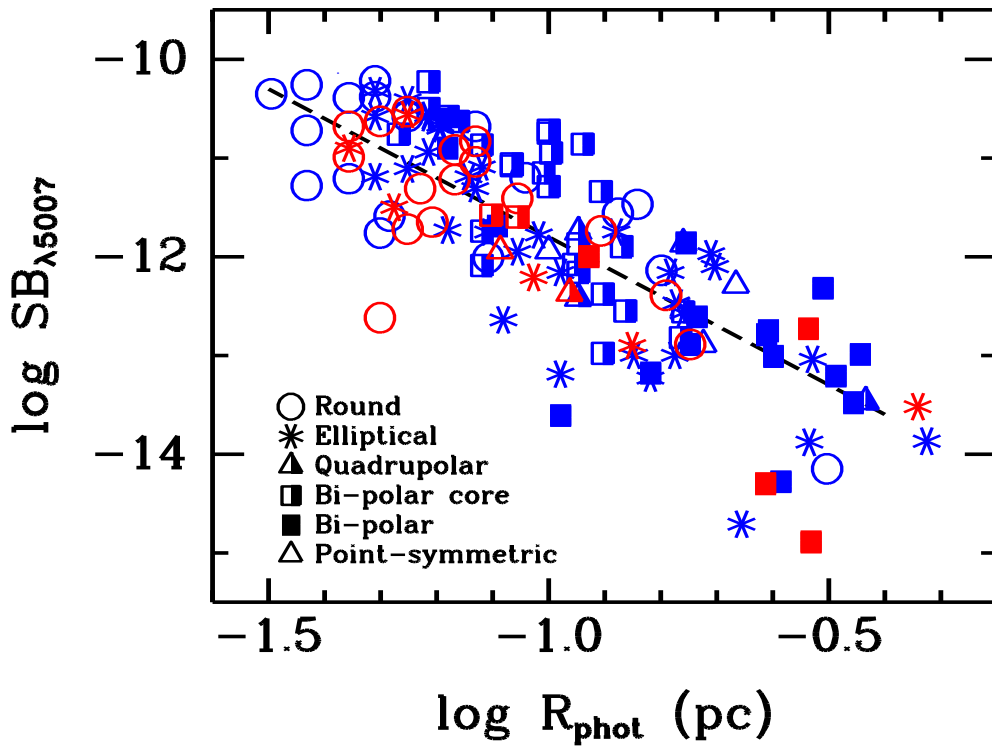


Fig. 23.— Decline of extinction-corrected, average surface brightness in [O III] $\lambda 5007$ ($SB_{[O III] \lambda 5007}$, in $\text{erg cm}^{-2} \text{s}^{-1} \text{arcsec}^{-2}$) with R_{phot} is consistent with an R^{-3} power law (*dotted line*). The various morphological types are represented by different symbols, as in Fig. 22 and in the legend. The electronic version of this paper shows LMC PNe in blue symbols, and SMC PNe in red.

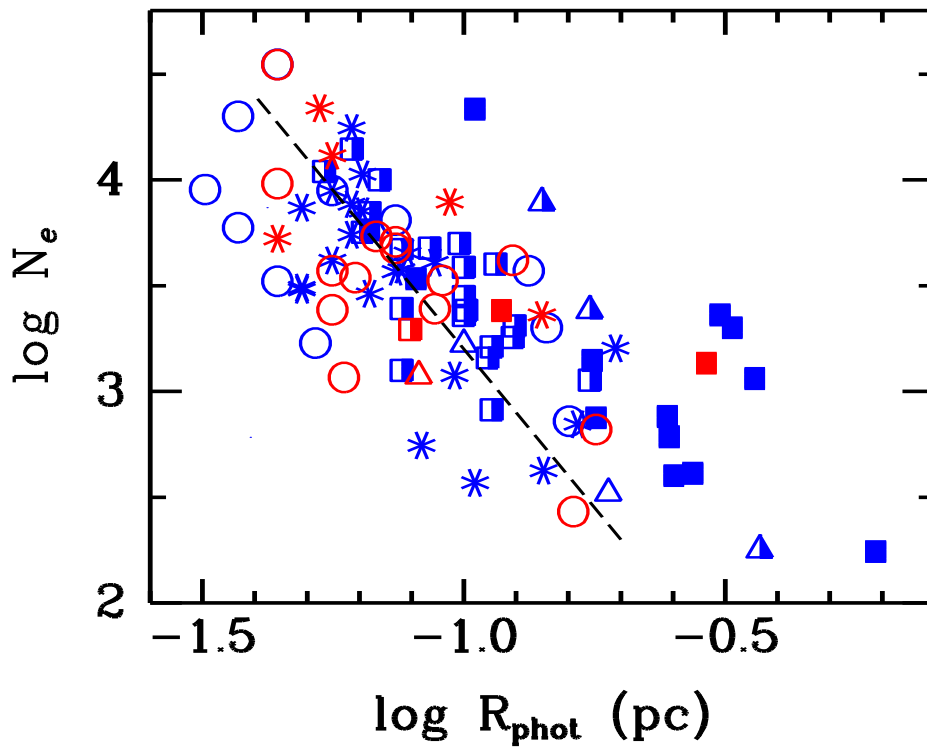


Fig. 24.— Nebular electron density vs. nebular (photometric) radius in pc. The nebular morphological types are represented with symbols as in Fig. 22. Dashed line shows an example decline in N_e as R^{-3} . The electronic version of this paper shows LMC PNe in blue symbols, and SMC PNe in red.

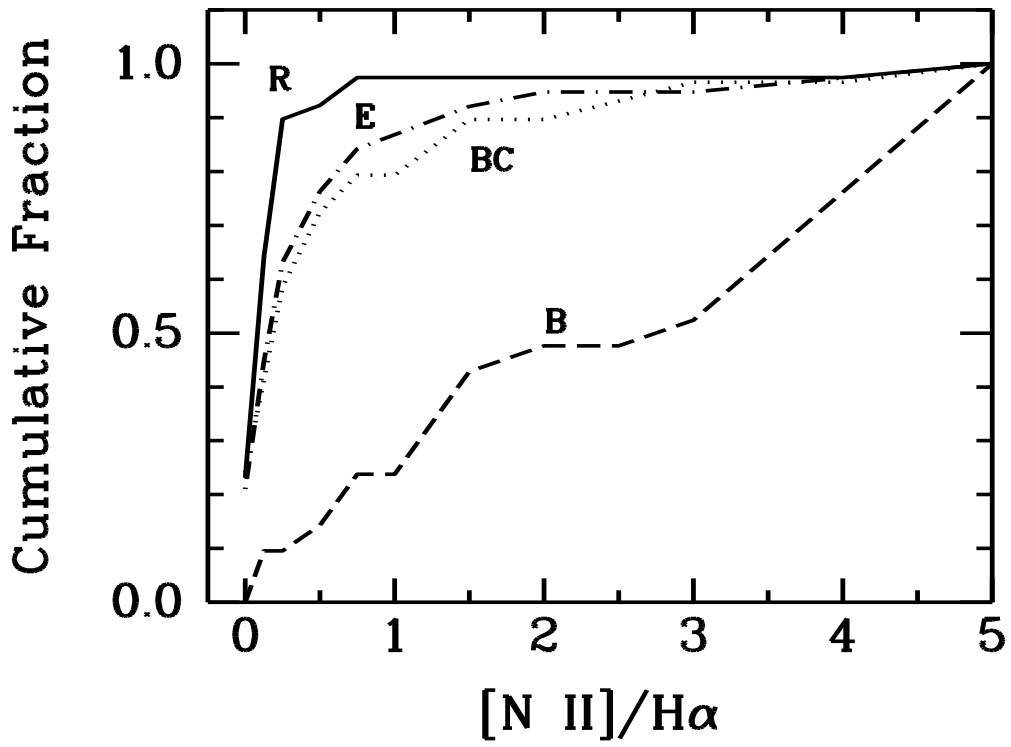


Fig. 25.— Cumulative fraction of PNe as a function of the flux ratio $F([\text{N II}])/F(\text{H}\alpha)$ (see text) for each morphological type: Round (*solid*), Elliptical (*dot-dash*), Bi-polar Core (*dotted*), and Bipolar (*dashed*).

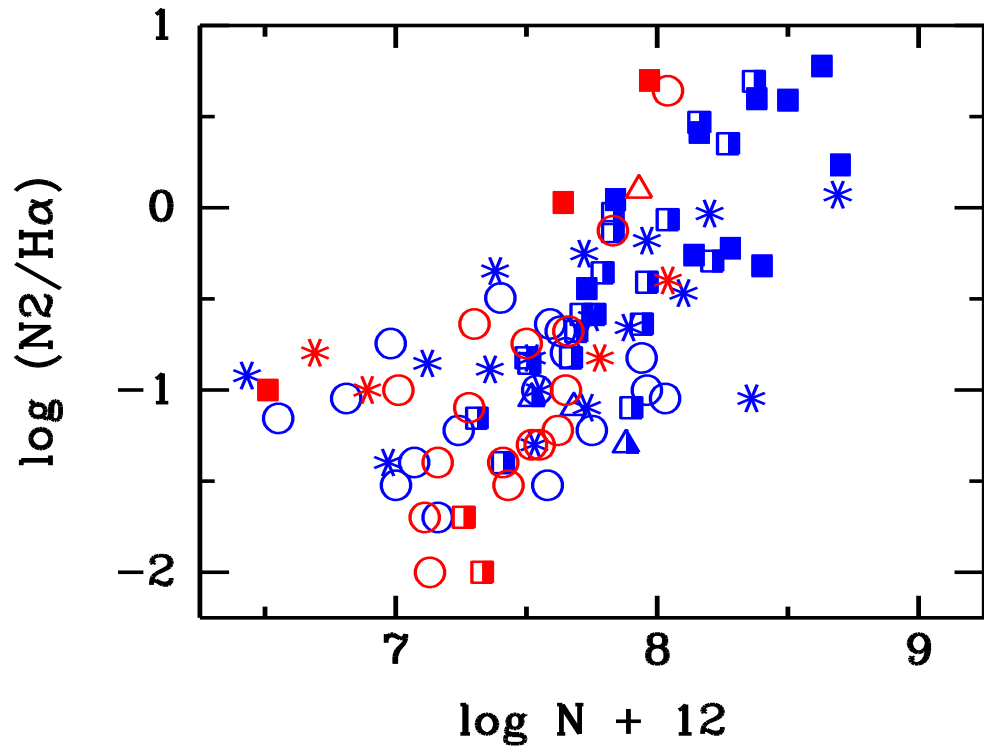


Fig. 26.— $F([N II])/F(H\alpha)$ vs. N for the LMC and SMC nebulae. The N abundances were taken from Stasinska, Richer, & Mc Call (1998); Leisy & Dennefeld (1996), and Meatheringham & Dopita (1991a,b). Symbols indicate morphological type, as in Fig. 23. The electronic version of this paper shows LMC PNe in blue symbols, and SMC PNe in red.

This figure "f4.jpg" is available in "jpg" format from:

<http://arxiv.org/ps/astro-ph/0608300>

This figure "f5.jpg" is available in "jpg" format from:

<http://arxiv.org/ps/astro-ph/0608300>

This figure "f6.jpg" is available in "jpg" format from:

<http://arxiv.org/ps/astro-ph/0608300>

This figure "f7.jpg" is available in "jpg" format from:

<http://arxiv.org/ps/astro-ph/0608300>

This figure "f8.jpg" is available in "jpg" format from:

<http://arxiv.org/ps/astro-ph/0608300>

This figure "f9.jpg" is available in "jpg" format from:

<http://arxiv.org/ps/astro-ph/0608300>

This figure "f10.jpg" is available in "jpg" format from:

<http://arxiv.org/ps/astro-ph/0608300>

This figure "f11.jpg" is available in "jpg" format from:

<http://arxiv.org/ps/astro-ph/0608300>

This figure "f12.jpg" is available in "jpg" format from:

<http://arxiv.org/ps/astro-ph/0608300>

This figure "f13.jpg" is available in "jpg" format from:

<http://arxiv.org/ps/astro-ph/0608300>

This figure "f14.jpg" is available in "jpg" format from:

<http://arxiv.org/ps/astro-ph/0608300>

This figure "f15.jpg" is available in "jpg" format from:

<http://arxiv.org/ps/astro-ph/0608300>

This figure "f16.jpg" is available in "jpg" format from:

<http://arxiv.org/ps/astro-ph/0608300>

This figure "f17.jpg" is available in "jpg" format from:

<http://arxiv.org/ps/astro-ph/0608300>

This figure "f18.jpg" is available in "jpg" format from:

<http://arxiv.org/ps/astro-ph/0608300>

This figure "f19.jpg" is available in "jpg" format from:

<http://arxiv.org/ps/astro-ph/0608300>